2016

Expandable Proppants for Hydraulic Fracturing

Livio Yang Santos
Louisiana State University and Agricultural and Mechanical College, lsanto4@lsu.edu

EXPANDABLE PROPPANTS FOR HYDRAULIC FRACTURING

A Thesis

Submitted to the Graduate Faculty of the
Louisiana State University and
Agricultural and Mechanical College
in partial fulfillment of the
requirements for the degree of
Master of Science

in

The Craft & Hawkins Department of Petroleum Engineering

by
Livio Santos
B.S. in University of Sao Paulo, 2010
December 2016

Acknowledgments

This thesis would not be possible without several contributions. It is a pleasure to thank Dr. Arash Dahi for the opportunity to work in this project and for giving me guidance and resources to complete this work. I am also sincerely grateful to my committee members, Dr. Guoqiang Li and Dr. Karsten Thompson, for sharing their truthful and illuminating views about this work.

I would like to acknowledge Coordination for the Improvement of Higher Educational Personnel (CAPES) for giving me the opportunity and the funding to pursue the master's degree in the United States.

I also thank all my friends for their friendship and support during this period. My heartfelt thanks to my family for their unconditional love and support.

Table of Contents

List of Tables

List of Figures

Abstract

Hydraulic fracturing is recognized as the primary technique to achieve economic oil and gas production from low permeability reservoirs like shale and tight-sand formations. One of the main challenges facing the oil and gas industry is maintaining the proppant functionality in the subsurface where replacement of proppant is only possible by expensive refracturing operations. Proppant crushing and proppant embedment have posed challenges for sustainable production from stimulated wells especially in soft and deep formations like Haynesville Shales. Experimental measurements show the strong impact of proppant stress and proppant embedment on reducing fracture conductivity.

In this work, we introduce a new class of smart "Expandable Proppants" (EP) to remotely control the expanding force and maintain the functionality of injected placed proppants. Our smart proppants are made out of thermoset shape memory polymers which are activated by formations in situ temperature to effectively maintain or even increase fractures width. A fully coupled CFD-DEM model is developed to study the effectiveness of expandable proppants and evaluate fracture conductivity enhancement via different combination and distribution of EP. In addition, a series of experiments were conducted in a modified API conductivity cell to measure the increase in fracture conductivity. Different conditions of temperature, confining stress, proppant size and concentrations are carried out to verify the optimum conditions.

Chapter 1
Introduction

1.1 Background

This research includes experimental measurement and numerical analysis to investigate effectiveness of expandable proppants made out of the shape memory polymers for hydraulic fracturing treatments. Hydraulic fracturing has helped the United States enhance its domestic energy supplies by shifting hydrocarbon production in places that were not considerate viable in the past. Nowadays, half of the oil production from the country comes from hydraulic fractured wells (approximately 4.5MMbbl/day) as presented in Figure 1.1.

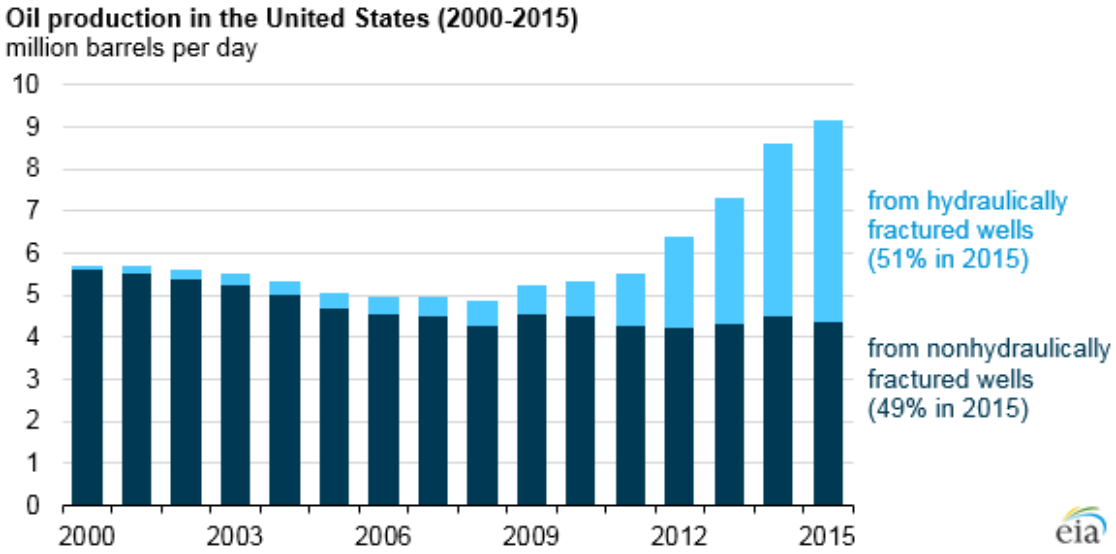

FIGURE 1.1. Comparative between oil production from hydraulic fractured wells and non-hydraulic fractured wells. (Source: US Energy Information Administration)

Proppants are solid materials required to hold fractures open after a hydraulic fracturing treatment. The primary purpose of the induced fractures is to increase the permeability of the rock and allow hydrocarbon production in formations of very low permeability, especially shale. Although sand is the proppant that is most

commonly used due to low costs and high availability, sand grains may collapse and generate fines when subjected to compressive stress. If not well consolidated, these fines can migrate and affect the permeability of the proppant bed. There are some treatments to avoid this type of problems and other materials such as ceramics or polymers can be used as proppant, for instance. Sand proppant is considered ideal for closure stresses up to 6000psi, while resin coat treated sands can resist to closure stresses up to 8000psi. Ceramic proppants depend on the sintered bauxite resistance and can resist to closure stresses of more than 10,000psi. Hence, proper proppant selection impacts hydrocarbon production in the long term, treatment size and job economics. Additionally, many other factors need to be considered, for example during production the effective stress is not constant, its value may increase with time (Zhang and Hou, 2014).

The fracture conductivity is the product of the permeability of the propping agent and the propped fracture width. Conductivity is a function of proppant properties (strength, size, composition, roundness, sphericity, distribution, concentration and content of fines), closure stress, pressure drawdown, and production rate. Fracture conductivity is considered as the most important factor for post operational performance and thus effectivity of hydraulic fracturing stimulation (Mader, 1989). Low conductivity can lead to low well productivity and potentially economical failure. In laboratory, fracture conductivity measurements can be performed in an API conductivity cell. The experiment consists in placing the proppant pack between two conductivity rock cores, simulating a fracture, and injecting fluid under different conditions of pressure and temperature.

The main factors affecting proppant pack permeability are fine generation, proppant crushing and proppant embedment (Fig. 1.2) into the formation. They all have been well documented in the literature. The variation in fracture conductivity can

reach two orders of magnitude, depending on the properties of the formation and the proppant pack (Fredd et al., 2001). Therefore, one of the key challenges in the industry is to predict the long term conductivity of the propped fractures. Plastic deformations and the effects of rock creep on hydraulic fractures in the long term are hard to be reproduced by experiments. Fracture conductivity tends to decrease over time and in extreme cases the induced fracture can even close. Such fact can take more than a year to occur while long term conductivity tests can last for only a few days.

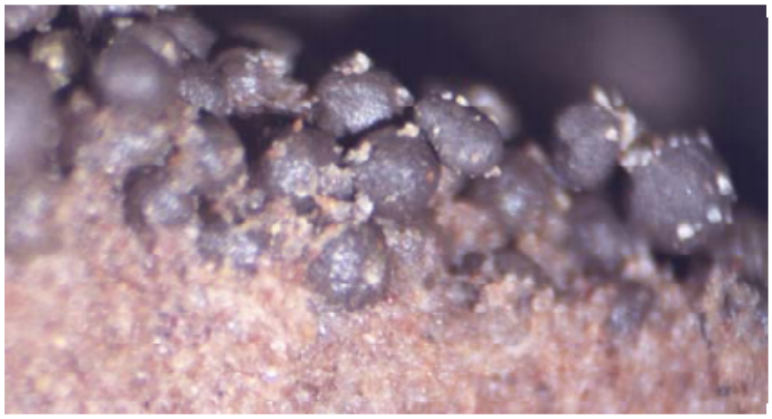

FIGURE 1.2. Proppant embedment into soft formations (Barree et al., 2003)

Lately, many improvements were made in proppants to increase their resistance to crush and embedment but they still cannot prevent the creep behavior from the formation. Based on these facts, we propose the utilization of a new material as proppant, a thermosetting polymer that can expand when placed in the fracture. The main purpose of the expansion of the proppant is to reduce and even cancel the effect of the creep behavior of the rock, responsible for rock closure. A series of experiments conducted with this proppant will be performed under different fracture widths, confining stresses, pressure and temperatures. Later, a discrete element model, based upon a granular simulator, of a proppant bed will be presented to simulate the same conditions as the experiment and verify the efficiency

of the new material as proppants. Considering proppants to be spheres, the model will be based on a soft contact model, largely applied to molecular simulations.

The studied proppants in this research are made out of shape memory polymers (SMPs). SMPs are a type of polymeric material that can be programmed to a different size and shape and then later return to the original shape. This change is activated by an external stimulus, such as light, heat or pH. The developed smart EP would respond to in-situ heating during its service conditions, without any need to halt production and refracturing the well. This smart EP has the capability to be programmed changing its conformational entropy, and its shape memory effect is activated through phase transformation by temperature, ultrasonic or electricity current. Fig. 1.3 shows a typical recording of the bottomhole pressure and temperature measurement during and after a typical fracture stimulation. Fluid and proppants have been pumped for a period of time. The termination of the pumping period is marked by a red line and followed by an extended period of shut-in that lasts much longer than the pumping time. Of particular interest here is that temperature of fracturing fluid and surrounding rock decrease till shut-in time. The following increase in temperature leads to activation of the smart proppants.

1.2 Motivation

In hydraulic fracturing operations, billions of grains (couple hundred thousands of pounds) are pumped along the fracking fluid. So small improvements in proppants are enough to enhance production of a hydraulic fractured well. Recent studies show that the operators have been investing more in high quality proppants and the industry is putting more effort on its development (Vincent et al., 2002). It is notorious that the global market size of the proppants is currently about 9 billion dollars while is not addressing the issues that can be solved by the proposed

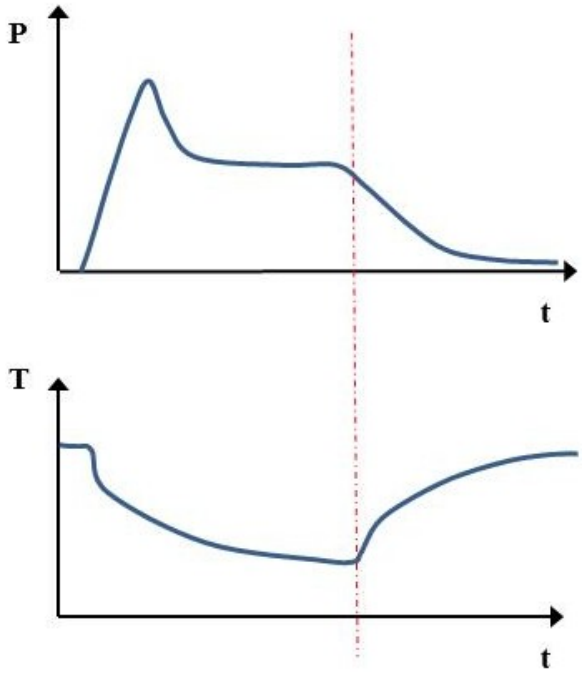

FIGURE 1.3. Bottomhole net pressure and temperature history during a typical fracturing treatment. Red line marks the end of pumping and, consequently, increase in temperature that would activate the EP.

expandable proppant. The developed smart EP would respond to in-situ heating during its service conditions, without any need to halt production and refracturing the well. In terms of economic perspective, it is notable that the combination of hydraulic fracturing and horizontal drilling technologies has enabled the production of oil and gas from tight sand and shale formations, also known as unconventional reservoirs. Shale gas has emerged as a major new energy source in North America in the past decade. In 2000, shale gas contributed only one percent to the U.S. natural gas production; this number grew to over 20 percent by 2010. Similar gains are being observed in Canada, and promising shale gas resources are being investigated now in China.

The market pain point in recovering oil and gas from shale plays is the fast and sudden drop in production due to post-treatment fracture closure. In other words, in some soft shale plays, hydrocarbon production in fractured wells show

no difference from non-fractured wells after a few months of production. Among different shale plays in North America, the most distinguishable ones with proppant related challenges are Haynesville shale, Eagleford shale, Tuscaloosa Marine Shale and Woodford shale which are contributing to 42% of current natural gas produced in the United States.

1.3 Research Objectives

The research objectives of this work are listed as below

1. To conduct experiments to verify the applicability of the shape memory polymers (SMPs) as proppant for hydraulic fracturing treatments.
   (a) To design the experimental apparatus for fracture conductivity measurement following modified API RP 61 (Recommended Practices for Evaluating Short Term Proppant Pack Conductivity).
   (b) To build the experimental apparatus to measure the hydraulic conductivity of regular and expandable proppants.
   (c) To run hydraulic conductivity experiments under different closure stresses to understand the potential impacts of the reservoir temperature and its closure stresses.
   (d) To test proppant samples with different grain size distributions, Young's modulus, strength, and activation temperature to achieve more optimal proppant selection.
2. To simulate proppant-pack conductivity using fully coupled computational fluid dynamics - discrete element methods.
   (a) To model the proppant-pack expansion in LIGGGHTS (Lammps Improved for General Granular and Granular Heat Transfer Simulations).
   (b) To calculate fracture conductivity due to proppant expansion using coupling of discrete element methods with computational fluid dynamics.
   (c) To validate simulation results with the lab experiment measurements.
   (d) To conduct virtual experiments to determine more effective proppant size and size distribution to achieve a higher proppant-bed permeability for given stress conditions.
3. To integrate numerical simulation into lab experiments to improve SMP design as proppant and save time and costs .
   (a) Predict the behavior of the fracture conductivity values based on the results of tests and simulations.

(b) To implement a fracturing job design and predict the well performance with SMP as propping agent.

Chapter 2
Theory and Literature Review

This section provides a review on the experimental methodology to measure fracture conductivity. The influence of the parameters, such as temperature, closure stress, time and proppant size are discussed based on the results acquired from previous studies. A brief review on shape memory polymers is also presented in the end of this section.

2.1 Fracture Conductivity

The main objective of hydraulic fracturing is to create a highly conductive flow path for hydrocarbon production. When this flow path is created, proppants are injected to assure that the popped fracture will not close. Fracture conductivity measures can be performed in laboratory and have been under investigation since the development of fracturing techniques. Cooke (1973) was one of the first to measure proppant pack permeability by using a conductivity cell. While previous experiments neglected temperature and flow rate effects, Cooke investigated both factors in a vertical fracture filled with proppants in the conductivity cell. The schematic of the apparatus can be seen in Figure 2.1. Data was obtained by applying closure stress with two pistons directly to the proppant pack for one hour under low flow rates, to avoid non-Darcy effects. Through his investigations he came to a conclusion that fracture conductivity has an inverse relationship with reservoir temperature and closure stress. Also, the author indicated the importance of non-Darcy flow at high gas flow rates and pointed that for extended times the permeability would certainly decrease.

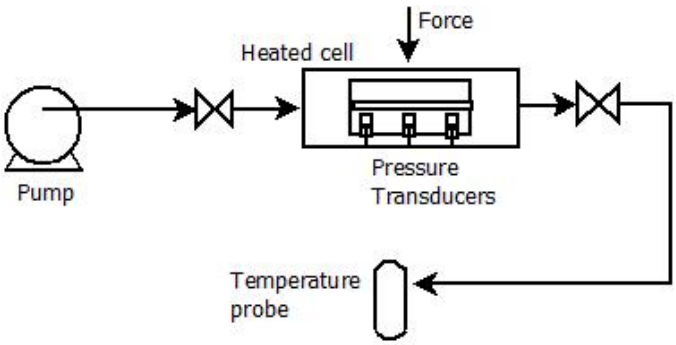

FIGURE 2.1. Schematic of the conductivity cell built by Cooke

Later, Cooke (1975) also evaluated the effects of fracturing fluids on fracture conductivity. One of the additives of the fracturing fluid has the purpose to seal pore spaces at the rock to avoid fluid loss but could potentially affect permeability. By placing two rock cores this time to simulate a fracture wall and filling them with proppant, he found that the effects of these fluid additives are negligible. In addition, that conductivity reduction is strongly related to the concentration and porosity of the proppant pack.

McDaniel (1986) extended the experiments duration from one to 18 hours to observe the decrease in fracture conductivity. He also tested different proppant sizes and variations in temperature and closure stress. As a result, conductivity decreased by an order of three in extended tests.

A different approach was introduced by Penny (1987), the author used multiple cells to evaluate proppant pack conductivity using dynamic testing. That means that instead of placing the proppant manually in the core, the proppant is pumped along with the fracture fluid, dynamically placing the proppant at the fracture, just like in the field. A wide variety of proppants were tested, including sands, resin coted sands and ceramic. Embedment, temperature and time of closure showed big effects on proppant permeability and conductivity.

In 1989, the procedures, apparatus and conditions for conductivity measurement in a conductivity cell were developed by American Petroleum Institute (API) and documented in API RP 61 (Marpaung et al., 2008). This method considers short term proppant pack conductivity. Since the introduction of the procedure, it has become standard for propped hydraulic fracture conductivity in laboratory measurements. Recent advances in technology combined with the need of acquisition of more realistic data leaded to the creation of new standards for measuring proppant conductivity. In 2001, International Organization for Standardization (ISO) and API formed a committee to define new procedures (Kaufman et al., 2007). The main modification is the inclusion of the long term conductivity test, where the time settled is 50 hours, which was established as time when the proppant pack reaches a semi-steady state.

Laboratory experiments conducted by Milton-Taylor (1992) verified the impact of fracture width on fracture stability. The results show that width up to six proppant diameters can keep the proppant pack stable and avoid proppant production. Although the experiments ignored some parameters, this rule was successfully applied to several hydraulic fracture treatments. However, factures can take more time to close. Blauer (1997) performed tests in sandstone to verify the effects of fracture closure. He observed that the fractures start closing after 90 days.

Numerical simulations of hydraulic fracturing treatments in naturally fractured reservoirs have shown that fracture opening at the intersection of fractures is prone to larger amount of compressional stress in comparison to the rest of the induced fracture (Dahi Taleghani and Olson, 2014; Dahi Taleghani, 2010). The strong compressional stress at the intersection (branching) point may reduce fracture conducitivity at these points, hence branching points may act as bottleneck during the production life of the wellbore (Asala et al., 2016).

The formation generated fines have big impact in the proppant pack permeability, plugging pores when they are submitted to high pressure and flow rate conditions. In order to prevent fines from entering the proppant pack and assure sustained conductivity during production the grains can be treated with a surface modification agent (SMA). SMA can be formulated using liquid resin to consolidate the proppant pack. In addition, resins increase the consolidation of the proppant pack and avoid proppant production. A 10 to 30% increase in conductivity occurs in laboratory experiments in the conductivity cell using SMA-treated proppant (Dewprashad et al., 1999). The treatment has to be planned carefully because the resin is very sensitive to pressure and temperature. In 1996, an epoxy resin treatment was able to eliminate proppant production of 14 out of 22 gas wells in the Hugoton gas field in North America (Cole, Amundson, and Allen, 1999).

2.2 Numerical Model

Considerable time and efforts are required for conducting experiments, thus we tried to developed some numerical tools to simulate the performance of SMP EP. Having a robust numerical tool will give us an opportunity to come with more effective and optimal utilization of EP for field application before field trials. Considering the nature of this problem, we chose Discrete Element Methods (DEM) to simulate the proppant bed permeability before and after activation, which includes study of particles individual motion, tracking their location, temperature changes, as well as tectonic forces and deformations associated with each step. Instead of a continuum, DEM considers granular materials as a collection of distinct particles. The energy is directly transferred between elements and their movement is tracked individually. By combining this technique with Computational Fluid Dynamics (CFD), it is possible to model the fluid flow through the proppant pack. Tsuji el al. (1993) was the first to implement a CFD-DEM model, followed then by so many

others. The authors carried out a 2-D model of a gas-solid fluidized bed of spherical particles. There are other methods to simulate fluid-particle interaction but considering computational efficency and numerical convenience, CFD-DEM has proved to be advantageous over other approaches such as Direct Numerical Simulations coupled with DEM (DNS-DEM) or Lattice Boltzmann Method coupled with DEM (LBM-DEM) (Zhu et al., 2007).

Previous works used the discrete approach to model proppant behaviour in a fracture. Mattson et al. (2014) built a 2-D DEM model to investigate the rearrangement of proppants in an API conductivity cell. The rearrangement causes non-uniform stress distribution along the cell and may overestimate fracture conductivity values. Asgian et al. (1995) conducted a numerical study to evaluate proppant flowback, an undesired condition where some some of the proppant is produced along the hydrocarbon. Performing eight simulations in DEM he verified which proppant properties and closures stress are more sensitive to proppant production. Later Shor and Sharma (2014) extended this work to a wider rage of confining stresses. Through their simulations they were able to quantify the dependence of proppant flowback on confining stress and proppant size. These works, though, use a drag force in DEM to simulate the fluid-particle interaction.

A 3-D numerical model to evaluate fracture conductivity was proposed by Shamsi (2015), coupling DEM with Lattice Boltzmann Method (LBM). The proppant pack is modelled using DEM while LBM is used to calculate the interstitial fluid flow. LBM is an alternative to classic CFD methods, where the kinetic equation for the particle distribution function is solved instead of solving Navier-Stokes equations. In their work the fracture conductivity is computed for different proppant sizes distribution and different confining stresses. Deng (2014) developed a DEM code to study the interaction between shale and proppant. The code is also coupled with

CFD to simulate a hydraulic fracture. Different shale properties (Young's modulus) and proppant sizes were tested.

2.3 Shape Memory Polymers

Thermosetting polymers are chemically or physically cross-linked polymers, meaning they have chemical bonds linking one polymer chain to another. As examples: epoxy, vinyl ester, polyester etc. They depend on temperature and loading rate and, like most polymers, they are amorphous (Li, 2014). These kind of polymers show different behaviors at different temperatures. Thus, when heated to the glass transition region (T_g), the mobility of the molecules increase and the motion of the segments along the loading direction becomes possible. This property can be explained by the free volume theory. This means that the occupied volume does not change with temperature, but the interstitial free volume may change linearly with temperature. In addition, there is the hole free volume, that expands nonlinearly with temperature. Thermosetting polymers usually consist of two parts, the liquid resin and curing agent mixed together.

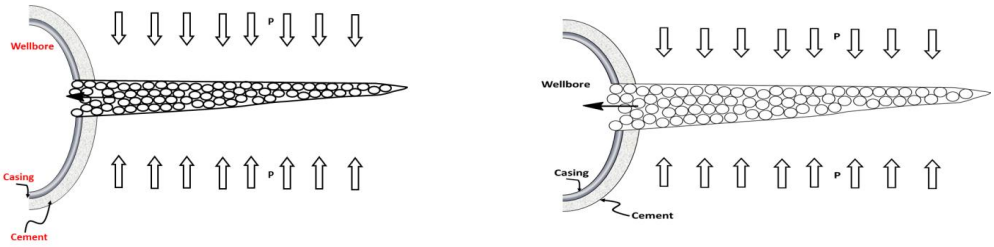

(a) Before (b) After

FIGURE 2.2. A popped fracture with smart proppants before and after the activation

Shape memory polymer was first developed in 1984, with the creation of the polynorbornene based SMP by the French company CDF Chimie Company (Xie, 2011). However, its application in the industry are recent due to new advances in

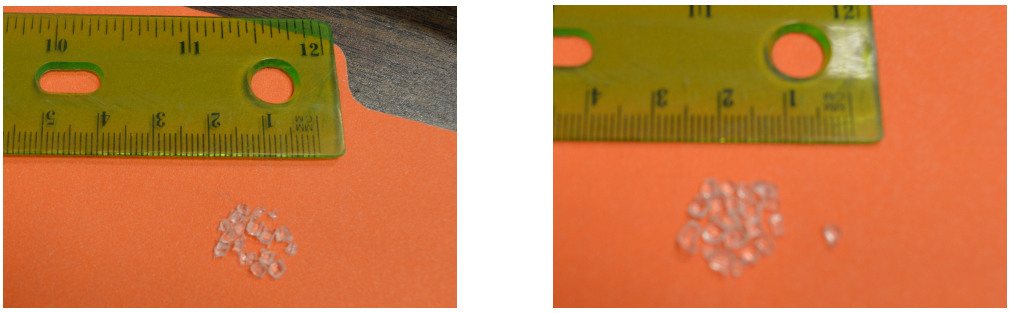

(a) (b)

FIGURE 2.3. Smart proppants a)Before activation; b)after activation

the field. The driving force for shape recovery is the conformational entropy of the molecular segments in terms of micro-Brownian thermal motion. With temperature increasing above T_g, there is a reduction in the viscosity and an increment in the molecule mobility, which leads to reel of molecules to their original configuration. Macroscopically, the polymer recovers to its original shape. Thermodynamically, the molecular segments experience a change from a temporary and ordered configuration to its random and coiled configuration during the shape recovery process. Since this process is accompanied by an increase in entropy, the process an autonomous (Li, 2014).

They are part of a smart class of materials with shape memory effect, along with shape memory ceramic and shape memory alloy, but have the advantage of being cheap, easier to process, non-toxic, biodegradable and can achieve much higher degrees of deformation (Li, 2014). Such characteristics made them ideal for many applications, including medical devices, sports clothing, temperature sensors, connectors and shrinkable tubes, for instance (Baghani, Mohammadi, and Naghdabadi, 2014). SMP foam has been used as a sand management alternative to gravel packing, the screen can shrink up to 70% of its original size when in place to prevent sand production (Carrejo, Johnson, and Horner, 2011). In a recent study by Dahi Taleghani et al. (2016), SMP particles are used as an expansive cement

additive to seal cement voids and fractures in the well annulus. The application of SMP particles in the petroleum industry can be considered unprecedented and a clear understanding of the SMP thermomechanical behaviour is critical to ensure a good proppant pack permeability during oil and gas production.

SMPs need to be programmed to change into the memorized shape and return to the original shape. The classical programming method is presented in Fig. 2.4, and it is a four step thermomechanical cycle, involving changes in temperature (T), stress (σ) and strain (ε). The process starts at temperatures above T_g, applying a high strain deformation (pre-deformation, or pre-strain). Then it is followed by the maintenance of the pre-strain while cooling down below T_g. The third step is the removal of the stress in the glassy state. After that, reheating the SMP to its initial temperature without applying constraint, brings the pre strain back to zero (unconstrained recovery) and recovers the initial shape. This is defined as free shape recovery. The low temperature unloading process may be accompanied by spring back, which is pre-strain rebounded. The amount of spring back reflects the shape fixity capability of the polymer. The shape fixity ratio can also be calculated. After the deformation the entropy will reduce (negative entropy change).

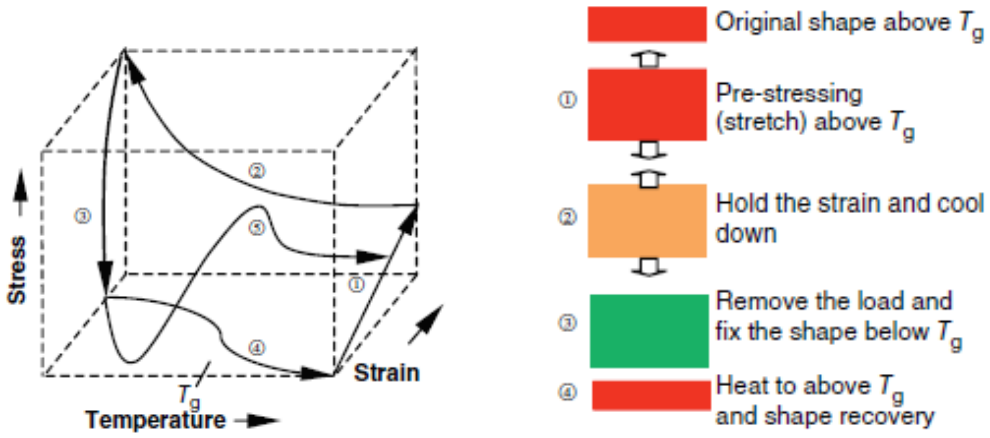

(a) (b)

FIGURE 2.4. a)Schematic of the classical programming method; b)Procedures to program SMP (Li, 2014)

Chapter 3
Materials and Experimental Procedure

The objective of running experiments is to reproduce field conditions in a hydraulic fracturing treatment in a very smaller scale. This chapter describes the equipment built to evaluate fracture conductivity, the material used and the procedures.

3.1 Experimental Setup

The equipment and materials used in the experiment are listed below (see figures 6.1, 6.2, 6.3 and 6.4 in Appendix A for more details)

- Sieve shaker (W. S. Tyler Ro-Tap RX-29)
- High pressure syringe pump (Teledyne Isco 500D)
- Modified RP-61 conductivity cell and 2 sandstone rock core samples
- Silicon heat tape, to heat to cell up to 400^{o}F (Briskheat)
- Load frame (Dake B-10)
- 3 Pressure transducers to measure the absolute and differential pressure across the cell
- Thermocouple to measure the temperature inside the cell
- NI USB 6000 data acquisition system
- NI USB-TC01 data acquisition system

3.1.1 Conductivity cell

The fracture conductivity cell consists of a cell body made of 316 grade stainless steel (Fig. 3.1) and two side pistons to hold the cores and apply confining stress (Fig. 3.2). The proppant is placed between the cores inside the cell, simulating a popped fracture. At the ends of the cell there is an inlet and an outlet port, allowing test fluid to flown along the cell body by the pump at a defined constant flow rate. On one side of the cell, three pressure transducers are connected to the

pressure ports. The transducer in the middle measures the absolute cell pressure, while the other two measures pressure across the cell (inlet and outlet pressures) at regular time steps. Filters are used to prevent the slurry from entering the pressure ports and protect the sensors. The filters used have a 140 microns screen.

On the other side, the port in the middle is connected to a thermocouple, which measure temperature inside the cell. Rupture disks are connected to the other two ports to ensure that the pressure inside the cell do not surpass 3000psi. The apparatus need to be in the load frame and carefully positioned at the center of the equipment so that stress is applied uniformly.

FIGURE 3.1. Conductivity cell loaded with smart proppants

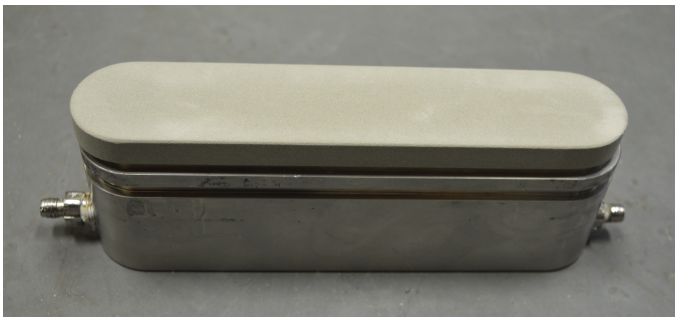

FIGURE 3.2. Side piston and sandstone conductivity core

3.1.2 Data Acquisition System

Honeywell pressure transducers were used to record the pressure evolution data along the pressure cells with two transducers on each cell. All pressure transducers were calibrated using a dead weight tester (Ashcroft 1305D as shown in Fig. 6.3a) to ensure proper pressure measurements. The dead weight tester apparatus uses identifiable weights to apply pressure to a fluid to verify and adjust the accuracy of the readings of the pressure transducers. The pressure transducers are connected to NI USB 6000 data acquisition system.

The thermocouple used are type K, from Omega. A thermocouple produces a temperature-dependent voltage as a result of the thermoelectric effect. This voltage is measured by the NI USB-TC01 data acquisition system and interpreted to measure temperature. All measurements are recorded by National Instruments' proprietary software LabVIEW.

3.1.3 Syringe Pump

High pressure syringe pump Teledyne Isco 500D was used to ensure constant flow rate. It is capable of providing flow rates from 0.001 to 204 ml/min and can store up to 507ml of fluid. The pump can produce pressures up to 3750psi. The pump is shown in Fig. 6.1 in appendix A.

3.2 Experimental Conditions

The experiments were performed following *API RP 61, Recommended Practices for Evaluating Short Term Proppant Pack Conductivity* 1989.

3.2.1 Proppants

Proppants have to be sieved because depending of the size, shape and distribution of the particles, there may be errors or variability involved in sampling due segregation. These particles tend to naturally find the path with less resistance when a force is applied (Kaufman et al., 2007). So firstly, the proppant sample is placed in

a sieve shaker, with 7 sieves with mesh distribution between 20-120 mesh, for 10 minutes to obtain particles with uniform sizes. Mesh is a measure of particle size distribution of granular material and the sieve sizes are regulated by standards. The sieves used in this experiment were:

The proppants are made of SMPs and are loaded in the cell with concentration of 2lbm/ft^2 ($9.76kg/m^2$). As the density of the proppants is $950kg/m^2$, we loaded the cell with $0.063kg$ of proppants. High concentration leads to wider propped fractures so slurry concentrations are usually designed to be above 1 lbm/ft^2 (Economides, 1992).

3.2.2 Rock Cores

The conductivity core (7 in. long, 1.5in. wide and 0.4 in. high) chosen was the Ohio sandstone because of its low permeability, similar to a tight sand reservoir (around 0.010 mD).

3.2.3 Test Fluid

The test fluid used in this experiment is distilled water at room temperature, as recommended by API RP 61. The syringe pump ensure constant flow rate.

3.2.4 Confining Stress

The values for confining stress were set to 5, 10 and 15MPa, applied by the hydraulic press.

3.2.5 Temperature

The experiment starts at room temperature and then the cell is heated to 90^{o}C in order to reproduce reservoir conditions and activate the proppant expansion. Temperature have a large effect on proppant properties, and consequently on fracture conductivity.

TABLE 3.1. Test parameters

Closure Stress (MPa)	**Flow Rates (cm^3/min)**	**Time at Stress (h)**	**Temperatures (C^o)**
5	10.0	0.25	23, 90
10	10.0	0.25	23, 90
15	10.0	0.25	23, 90

3.3 Experimental Procedures

To begin the experiment, two sandstone cores (previously saturated) are assembled in the fracture conductivity cell, one in each piston of the fracture conductivity cell as show in Fig. 5b. The samples have a rectangular shape with rounded edges and they have to be wrapped in Teflon tape to prevent leakage. The bottom piston is inserted first, then, the proppant is placed between the cores, making sure that the fracture is in the middle of the conductivity cell. The quantity of proppant determines the fracture width and is important to measure the conductivity. The top core sample with the piston is inserted after with the aid of the hydraulic press. Once this setup is ready, the leak off port of the pistons need to be sealed. The heating tape is wrapped around the conductivity cell and adjusted to the desired temperature.

The next step is placing the cell in the center of the hydraulic press and pump until achieve the desired confining stress. The fracture width is measured with a calliper at each end of the test unit to make sure the level is uniform. After that, the conductivity cell is ready for the experiment. The inlet of the conductivity cell is then open and the pump can be started at a constant desired flow rate. Figs. 3.3, 3.4 and 3.5 show the LabVIEW screens to set the flow rate and monitor temperature and pressure, respectively. After accumulating some pressure and checking for leaks we open the outlet valve and wait for the pressure to stabilize. Pressure readings are recorded at regular intervals by the software. After 15 minutes we increase the

flow and record the pressure readings. The time is sufficient for the proppant bed to reach a semi-steady condition.

To verify the fracture conductivity of the expanded proppant we set the temperature in the heating tape to 90^o. The process can take up to one hour and, after that, we measure the fracture width and repeat the procedures described previously.

3.4 Fracture Conductivity Calculation

Under laminar conditions, the proppant pack conductivity is calculated using Darcys equation (considering the test unit width 1.5in and the length between the pressure ports 5in)

$$kW_f = \frac{26.78\mu Q}{\Delta P} \tag{3.1}$$

To calculate the proppant pack permeability use

$$k = \frac{321.4\mu Q}{\Delta P W_f} \tag{3.2}$$

Where k is the proppant pack permeability in mD, μ is the viscosity of test liquid at test temperature, in cP, Q denotes flowrate in cm^3/min, W_f is the pack width in inches and ΔP is the pressure drop in psi. Since the flow rate is very low, non-Darcy flow effects are negligible.

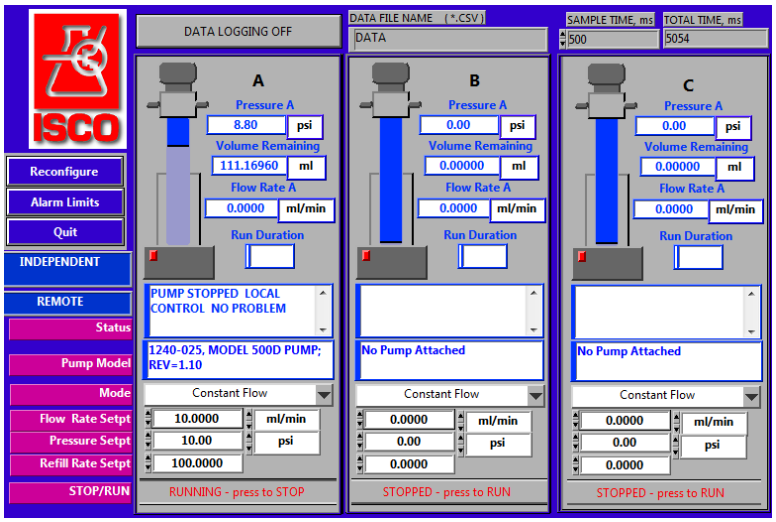

FIGURE 3.3. Pump settings

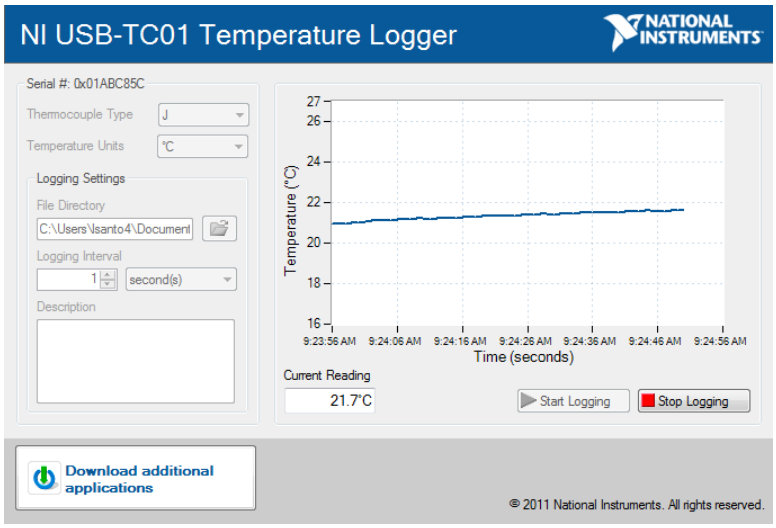

FIGURE 3.4. Temperature log

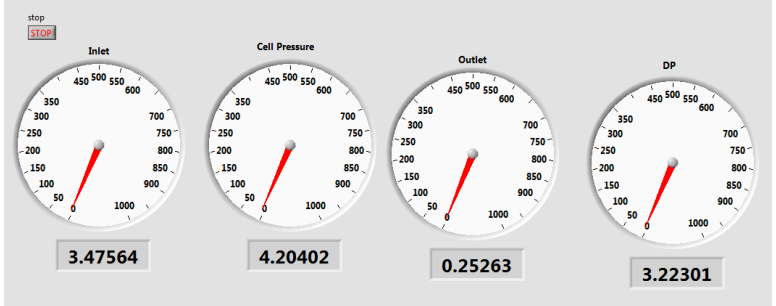

FIGURE 3.5. Instantaneous pressure readings

Chapter 4
Numerical Model Description

This chapter details the numerical model developed to verify the efficiency of the smart proppants. The interaction between particles and also between fluid and particles are thoroughly described.

4.1 Discrete Element Method (DEM)

Discrete element methods, also known as distinct element methods, is a numerical method to simulate motion and effect of granular particles. This model was proposed by Cundall in 1971 to solve rock mechanics problems and allow us to understand the underlying interactions between particles (Cundall and Strack, 1979). Although most particles are not spherical, the discrete model can be applied to study their mechanical behaviour. The interaction between particles occurs only at contact points and they are simulated individually, thus new contacts are recognized as the simulation progresses (Shor and Sharma, 2014). The time integration is done on a time scale much smaller than the typical contact time. These minor steps ensure that for each time step the disturbance do not propagate from the particle and fluid farther than its immediate neighbours. To describe the motion of each element, Newtons second law is applied. Below, the main steps to complete a DEM simulation are listed:

- Initialization: First, initial configuration of particles, geometry and boundary conditions are defined. Position, radius and shape of the particles (usually spheres).

- Application of forces: The contacting particles are identified, then force is calculated in each particle (pressure, gravity, friction caused by neighbour particles, for example).

- Force calculations: From the forces mentioned above, the resultant force and momentum or torque acting in each particle is computed, including body forces and external forces.

- Integration: The acceleration of each particle are calculated and integrated to define their velocities.

- Analysis: For each time step, mechanical and thermal parameters are computed. The previous steps are repeated until the solution is complete.

- Post processing: Generates output data and graphical visualization of the simulation.

Initially, the particle velocities and incremental displacements are computed considering equilibrium of each particle in sequence. Then, after updating the system geometry the force at contact points are calculated.

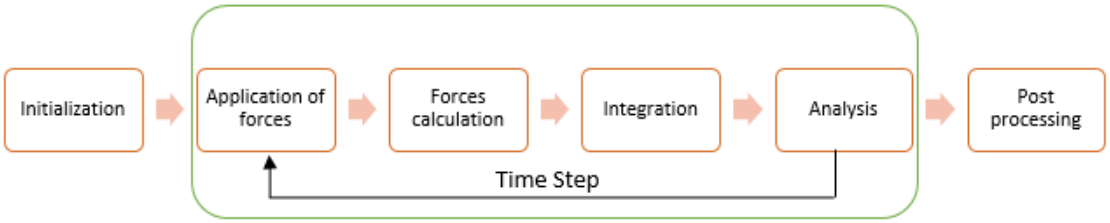

FIGURE 4.1. Flowchart of the steps to complete a DEM simulation

The model was built in a granular simulator, LIGGGHTS (LAMMMPS Improved for General Granular and Granular Heat Transfer Simulations, LAMMPS is an open source successful molecular dynamics code). Kloss (Kloss et al., 2012) describes the simulator thoroughly. LIGGGHTS is executed by reading the code from an input file, there is no graphical interface. After running the code, the software generates an output file for each time step, containing information of the position of the particles in that particular time step. These files have to be post processed so they can be visualized graphically.

4.1.1 Governing Equations

DEM is a Lagrangian method, which by definition means that the particles inside the domain are tracked by following their trajectories (Kloss et al., 2012). The governing equations for rotational and translational motions are

$$m_i \ddot{x}_i = F_{i,n} + F_{i,t} + F_{i,f} + F_{i,b} \tag{4.1}$$

$$I_i \frac{d\omega_i}{dt} = r_{i,c} \times F_{i,t} + T_{i,r} \tag{4.2}$$

Where $F_{i,n}$ denotes the normal particle-particle contact force, $F_{i,t}$ is the tangential particle-particle contact force, $F_{i,f}$ is particle-fluid interaction and $F_{i,b}$ is the sum of other forces such as gravity, electrostatic and magnetic. $T_{i,r}$ is the torque acting on the particle. The forces and torques are calculated on each particle position, thus equations 4.1 and 4.2 can give rotational and translational acceleration, $\dot{\omega}_i$ and $\ddot{x}_i$.

4.1.2 Contact Force Model

The soft sphere model considered for this work, unlike the hard sphere model, recognizes deformations and penetrations between spheres. The principle behind this model is to solve the equations guiding the angular and linear equilibrium of the spheres in minor steps. These spheres interact through a spatial overlap (Figure 4.2), which represents the particle deformation, causing transference of normal (F_n) and tangential forces (F_t) through a linear spring and dashpot model, as shown in Figure 4.3. The spring constants are function of the material and dampening properties are function of the viscosity of the medium (Shor and Sharma, 2014). As outlined by OSullivan (2011), the normal component is calculated considering either the particle overlap or separation (for compressive and tensile forces, respectively). Tangential forces are calculated from the cumulative relative displacement at contact points, in the orthogonal direction to normal orientation. Each element

interacts only with its neighbors because the simulator has neighbors list for each element.

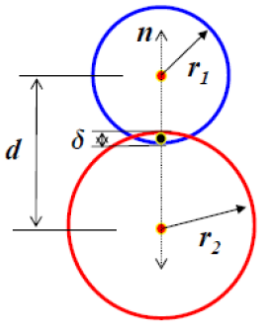

FIGURE 4.2. Overlap between particles, representing the deformation given by δ

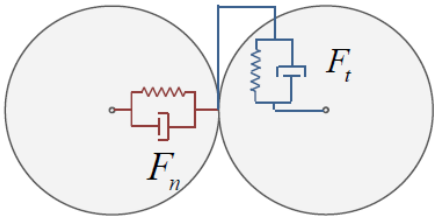

FIGURE 4.3. Linear spring dashpot model assumed for DEM, including a dissipative viscous dashpot at the contact point to account for energy dissipation due to plastic deformation

$$\vec{F_n} = k_n\vec{\delta} + c_n\overrightarrow{\Delta v_n} \tag{4.3}$$

$$\vec{F_t} = k_t|\int_{t_{c,0}}^{t} \Delta v_t(\tau)d\tau|\vec{t} + c_t\overrightarrow{\Delta v_t} \tag{4.4}$$

where Δv_n and Δv_t are normal relative velocity and tangential relative velocity at the contact point, respectively, t is tangential vector at the contact point, is time at which the contact begins. k_n and k_t are elastic constants for normal and tangential contacts and they are function of Youngs modulus and Poisson Ratio. C_n is the dissipative term.

The magnitude of the tangential force is bounded by the frictional force.

$$max(|\vec{F_t}|) = |\mu_c \vec{F_n}| \tag{4.5}$$

Where μ_c is the friction coefficient.

4.1.3 Particle-Particle heat transfer

The particleparticle heat conduction model is based on the work of Chaudhuri et al (2006), which describes heat transfer in three dimensional DEM. The work accounts for thermal conduction through the contact area between two particles in contact. The model considers initial material temperature, wall temperature, granular heat capacity, granular heat transfer coefficient and granular flow properties. The heat transfer simulations use a linear model. Assuming constant temperature within the particle for each time step, the energy equation for a particle is given by

$$m_i c_{p,j} \frac{dT_i}{dt} = \sum_j Q_{ij} + Q_{src,i} \tag{4.6}$$

Where T_i denotes particle temperature, $c_{p,j}$ is particle thermal capacity, Q_{ij} is heat flux between the particles and $Q_{src,i}$ is heat source for the particle.

$$Q_{ij} = H_{ij}(T_j - T_i) \tag{4.7}$$

H_{ij} is the heat transfer coefficient and it is calculated from the thermal conductivities and is given by

$$H_{ij} = 4\frac{k_i k_j}{k_i + k_j}\sqrt{A_{c,ij}} \tag{4.8}$$

and $A_{c,ij}$ is the contact area between the the particles

$$A_{c,ij} = -\frac{\pi}{4}\frac{(c_{ij} - r_i - r_j)(c_{ij} + r_i - r_j)(c_{ij} - r_i + r_j)(c_{ij} + r_i + r_j)}{c_{ij}^2} \tag{4.9}$$

where

$$c_{ij} = \delta_{n,ij} - r_i - r_j \tag{4.10}$$

4.2 Computational Fluid Dynamics

Computational fluid dynamics (CFD) is the study of systems involving fluid flow, heat transfer and associated fluid phenomena through computer-based simulations. This technique is very powerful and can be applied in a wide range of fields. CFD codes are composed of numerical algorithms to solve fluid flow problems and they are divided in three main parts. The first one is pre-processing, where the input data like the geometry, grid size, fluid properties, chemical and physical phenomena are defined. The second is the solver, which uses finite volume method (FVM) to evaluate PDE in the form of algebraic equations and then solve the algebraic equations by an iterative method. The values are calculated at discrete places on a meshed geometry, but the FVM is distinct from other techniques such as finite difference due to the integration of the governing equations over all the control volumes of the domain (Versteeg and Malalasekera, 2006). Finally, the post processing includes tools for data visualization.

We used the CFD framework OpenFOAM, which stands for "Open Source Field Operation and Manipulation. OpenFOAM is open source and has a wide variety of solvers, but our focus will be on incompressible steady-state flow.

4.3 Computational Fluid Dynamics Discrete Element Methods model

The CFD-DEM (Computational Fluid Dynamics Discrete Element Methods) model can couple solid particles simulations with fluid systems. In this research we used CFDEM coupling, an open source CFD-DEM engine, coupling LIGGGHTS with OpenFOAM. The software can simulate also momentum, heat and mass ex-

change between phases. The motion of the particles are modeled by solving Newtons equation in the discrete approach DEM, as described before, while the interstitial incompressible fluid flow uses the continuum approach CFD, based on local averaged Navier-Stokes equations, assuring conservation of momentum and mass (Zhu et al., 2007).

$$\frac{\partial \varepsilon_f}{\partial t} + \nabla.(\varepsilon_f u_f) = 0 \tag{4.11}$$

$$\frac{\partial (\varepsilon_f u_f)}{\partial t} + \nabla.(\epsilon_f u_f u_f) = \varepsilon_f \nabla \frac{p}{\rho_f} - R_{pf} + \nabla.\tau \tag{4.12}$$

where u_f and p are, respectively, the fluid velocity and pressure, τ, ε_f and R_{pf} are the fluid viscous stress tensor, volume fraction occupied by the fluid and momentum exchange with the particulate phase. Considering only the laminar conditions, the fluid moves in an orderly manner and maintain the same position relative to pipe bounding flow.

Equations 4.11 and 4.12 are solved using the PISO algorithm, which for numerical reasons divide the particle-fluid momentum exchange in implicit and explicit terms. This way

$$R_{pf} = K_{pf}(u_f - \langle u_p \rangle) \tag{4.13}$$

$$K_{pf} = \frac{\sum_i F_d}{V_{cell}|u_f - \langle u_p \rangle|} \tag{4.14}$$

where K_{pf} is the momentum exchange coefficient, $\langle u_p \rangle$ is a cell based enseble averaged particle velocity and F_d is the drag force, explained in the next section.

4.3.1 Fluid-Particle Interaction

Different types of forces act on particles submerged in fluids, hydrostatic or hydrodynamics (Zhu et al., 2007). The hydrostatic force is the buoyancy force due

to pressure gradient around the particle.

$$F_b = \frac{1}{6}\pi\rho d_p^3 g \tag{4.15}$$

Hydrodynamics forces include drag force, virtual mass force and lift force. The dominant fluid-particle force is the drag force (O'Sullivan, 2011), and it depends on a drag coefficient C_d, the particle fluid relative velocity and the particle diameter d_p. The drag force is defined usually by both theoretical analysis and fits to experimental data. The expression 4.16 was proposed by Di Felice (1994) and does not depend on the flow regime.

$$F_d = C_d \pi \rho_f d_p^2 |V_f - V_p| \frac{V_f - V_p}{8} \varepsilon^{1-\chi} \tag{4.16}$$

$$C_d = \left(0.63 + \frac{4.8}{\sqrt{R_p}}\right)^2 \tag{4.17}$$

$$R_p = \frac{\varepsilon \rho d_p |V_f - V_p|}{\mu} \tag{4.18}$$

$$\chi = 3.7 - 0.65 \exp\left[\frac{-(1.5 - \log R_p)^2}{2}\right] \tag{4.19}$$

Here, $\varepsilon^{-\chi}$ is a corrective function that consider other particles present in the system.

In the literature, there are three distinct formulations describing the particle-fluid flow, as described by Zhou et al. (2010). Besides theses forces, others forces have been neglected in this work, like Magnus force (particle rotation), Saffman force (fluid velocity gradient leading to shear) or pressure force (pressure gradient in the flow field.

The coupling of both models is calculated in time steps. For each time step, the position and velocities of the solid particles are given by DEM, then the information

is evaluated for porosity and drag force data in a computational cell. CFD can obtain the fluid flow from this data and incorporate the fluid drag forces on the individual particles, which will lead DEM to calculate the motion of the particles for the next time step (Yu and Xu, 2003; Zhu et al., 2007). This process follows Newtons third law of motion, which states that the force acting of the solid phase acting on the liquid phase should be equal to the force of the liquid phase acting on the solid phase but in the opposite direction.

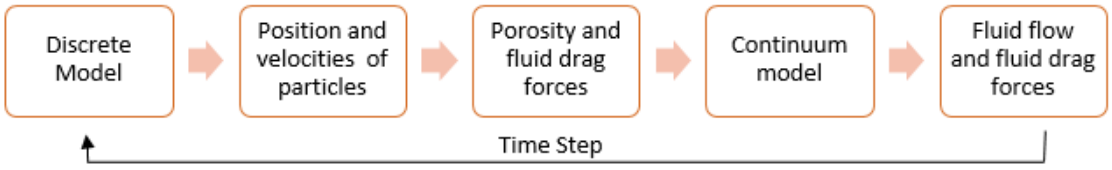

FIGURE 4.4. Simplified flowchart of the steps to complete a CFD-DEM simulation

The software allows two different approaches, the unresolved approach (Fig. 4.5a) where the particle sizes are smaller than the computational grid and the resolved approach (Fig.4.5b), with particles sizes bigger than the computational grid. The last one give more accurate flow calculations, but with greater computational expense due to the extra cells generated. n our simulations we used the unresolved approach. In this case, CFD and DEM time steps can be defined separately from each other. The DEM time steps need to be set at least one order of magnitude smaller than CFD because of the high intensity of particle collisions and overlapping (Kloss et al., 2012).

4.3.2 Fluid-Particle Heat-Transfer

The model for convective heat transfer between particulate phase and fluid phase is based on Li & Mason (2000) calculated by

$$\frac{\partial T_f}{\partial t} + \nabla.(T_f.u_f) = \nabla.(\kappa_{eff}\nabla T_f) + S_t \tag{4.20}$$

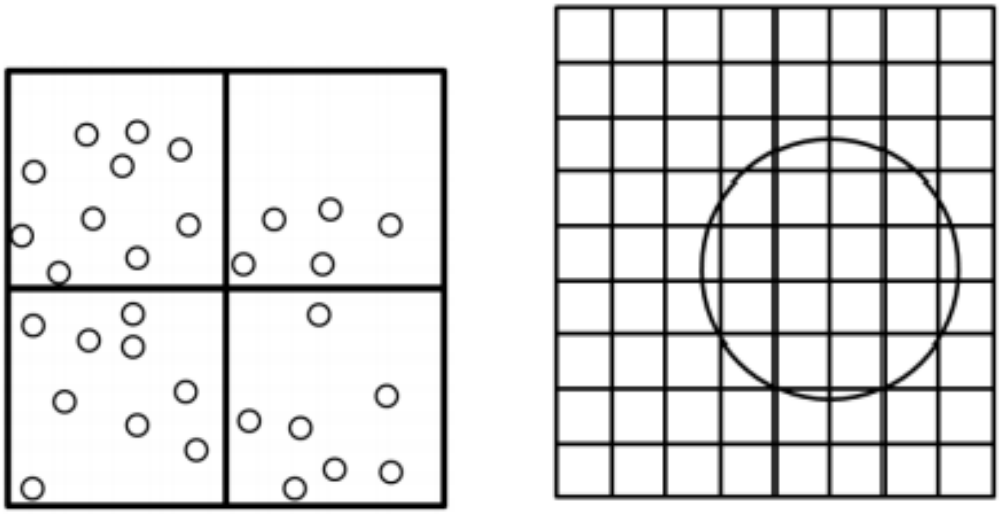

FIGURE 4.5. a)Unresolved CFD-DEM approach, where the computational grid is bigger than the particles; b)Resolved CFD-DEM approach, with the computational grid is smaller than the particles (Kloss et al., 2012)

Where κ is the thermal diffusivity and S_T is the source term given by

$$S_T = -\frac{q_p}{\rho_f C V_c ell} \tag{4.21}$$

q_p is the heat transfer ratio given by

$$q_p = hA_p(T_f - T_p) \tag{4.22}$$

And h is the heat transfer coefficient

$$h = \frac{\lambda Nu_p}{d_p} \tag{4.23}$$

Nu_p denotes the particle Nusselt number and is a function of the particle Reynolds number Re_p and the Prandtl number Pr. For $Re_p < 200$

$$Nu_p = 2 + 6r_p^{1/2} Pr^{1/3} \tag{4.24}$$

4.4 Simulation Procedure

The simulation involves the creation of a proppant pack, application of confining pressure from the formation, proppant expansion,and fluid flow in one direction.

1. A simulation region in DEM is defined. In order to minimze computational efforts a representative volume is taken. The fracture is represented by a rectangular box with 5.0mm in width, 5.0mm in height and 8.0mm in width.
2. A proppant pack is generated with a previously defined size (Table 4.1).
3. A normal force is applied by a servo controlled wall (z-direction) while the other walls remain immobile, with constant confining stress. The proppant pack consolidate under the applied external pressure that is mimicking formation closure stress.
4. Test fluid (water) is pumped in the x-direction, keeping a constant low flow rate. Inlet and outlet pressures are registered for regular interval of time steps.
5. Then, as the temperature increase, the proppant starts to expand.

The CFD-DEM solver used to solve the simulations was cfdemSolverPisoScalar which solves Navier-Stokes equation considering the momentum exchange and volume displacement of the particles, calculated by DEM. All simulations were run in a dual quad core processor Intel i7 with 15.6B of memory and can take up to 72 hours depending on the particle size.

The results are presented in plots that follow and show the response of the porosity, permeability and fracture width to confining stress. A verification case, comparing the numerical result to an analytical solution is run in order to check the accuracy of the model.

TABLE 4.1. Proppant size

Size	**Minimum diameter (mm)**	**Maximum Diameter (mm)**	**Particles**
12/20	0.85	1.41	98
16/30	0.6	1.0	318
20/40	0.425	0.71	950

Chapter 5
Results

In this chapter, the project results will be presented and discussed. The results are displayed in terms of porosity, permeability and fracture aperture under a range of confining stresses. The influence of proppant size and stiffness is also discussed.

5.1 Preliminary Analysis

The properties of the first samples of EP are listed in Table 5.1. Simulations under high compressive strength and with small particles have proven to be very lengthy. In order to reduce computational time, simulations were run with proppants mesh size 12/20, 16/30 and 20/40.

TABLE 5.1. EP parameters for the numerical simulations

Parameters	**Values**
Density (ρ)	950 kg/m^3
Young's Modulus (E)	260 MPa
Possion's Ratio (ν)	0.45
Friction coefficient (μ_c)	0.5

The proppant pack without expansion and under confining stress, generated by DEM simulations is shown in Fig. 5.1. In these examples the confining stress is 20 MPa.

Coupling CFD and DEM generates the fluid flow through the proppant bed. The temperature increment in the fluid and pressure differential are displayed in Fig. 5.2. It is important to notice that OpenFOAM works with kinematic pressure ($\frac{p}{\rho}$) and its units are $\frac{m^2}{s^2}$.

The parameters analysed in this study were porosity, permeability and fracture opening. Initial porosity is higher than the porosity of a packed bed of spheres due to the wall effect, the porosity increases when in contact with a solid boundary.

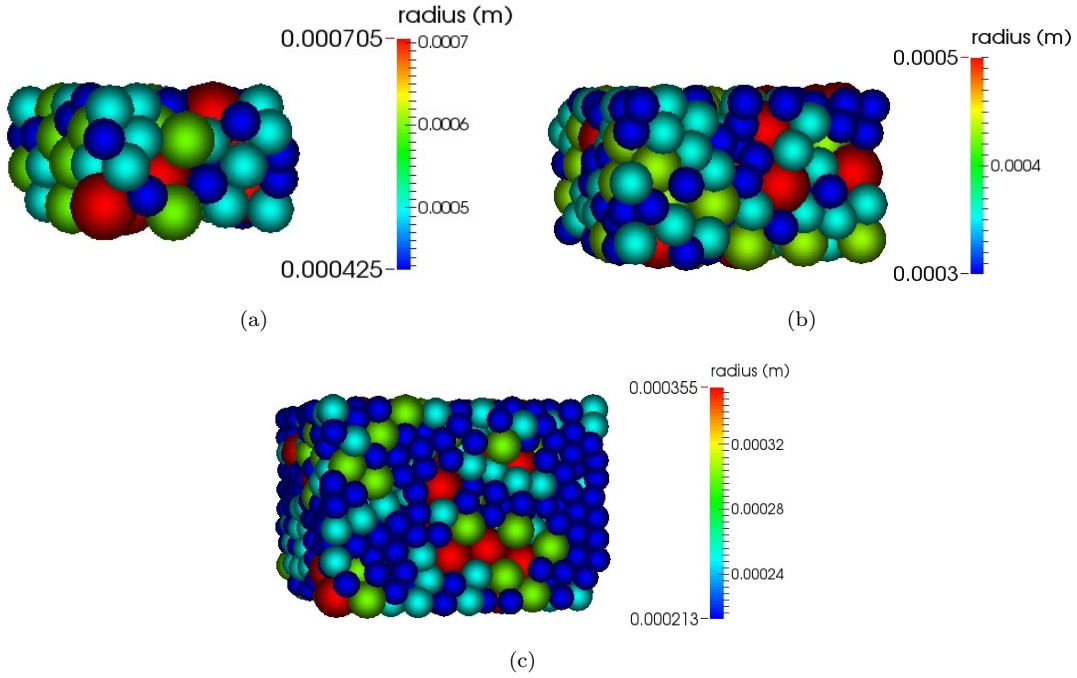

FIGURE 5.1. Different mesh sizes of proppant pack bed under confining stress a)12/20 b)16/30 c)20/40

Porosity is given by the void space of the CFD cell. As the proppants are compressible, the reduction in fracture width is not only due to closure of pore spaces. Preliminary results suggests that the particles are too soft our purpose. High proppant deformation under closure stresses were observed, causing a big decrease in porosity and permeability. These results can be seem in Figs. 5.3 and 5.4.

The same fact was observed in the experiments, where the compaction and following proppant expansion leaded to closure of the pores, as shown in Fig. 5.1. The proppants used in the experiments were also too large (around 2mm of diameter) so the results cannot be used in comparison with the numerical model. But the images can confirm the effect observed in the simulations

As observed in Fig. 9 for both cases at 20MPa confining stress, the porosity of the proppant pack is smaller than 10% and the permeability is smaller than 10 Darcy, which is not acceptable for proppants of this size and will not allow good flow. The permeability reduction under these high stresses are due to the deforma-

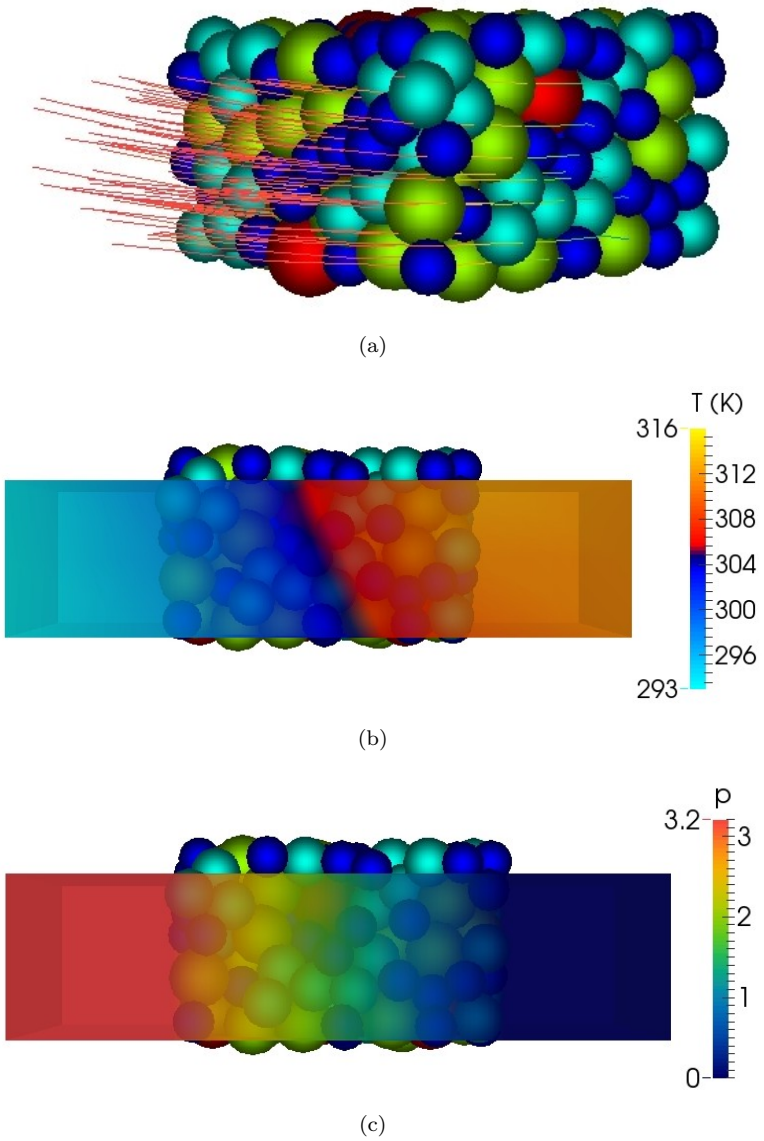

(a)

(b)

(c)

FIGURE 5.2. a)Stream lines representing the fluid flow through the proppant pack b)Fluid temperature increasing in the fracture c)Fluid pressure differential, allowing us to calculate fracture the permeability of the pack

tion the particle, reducing their sphericity and partially plugging the pore spaces. So, in addition to reduction in permeability, the fracture width also decreased substantially, resulting in large fracture conductivity reduction.

5.2 Incremented Young's Modulus

An attempt to obtain better results was made by increasing the Youngs modulus to 520MP. A clear indication of the improvement is the larger values obtained for

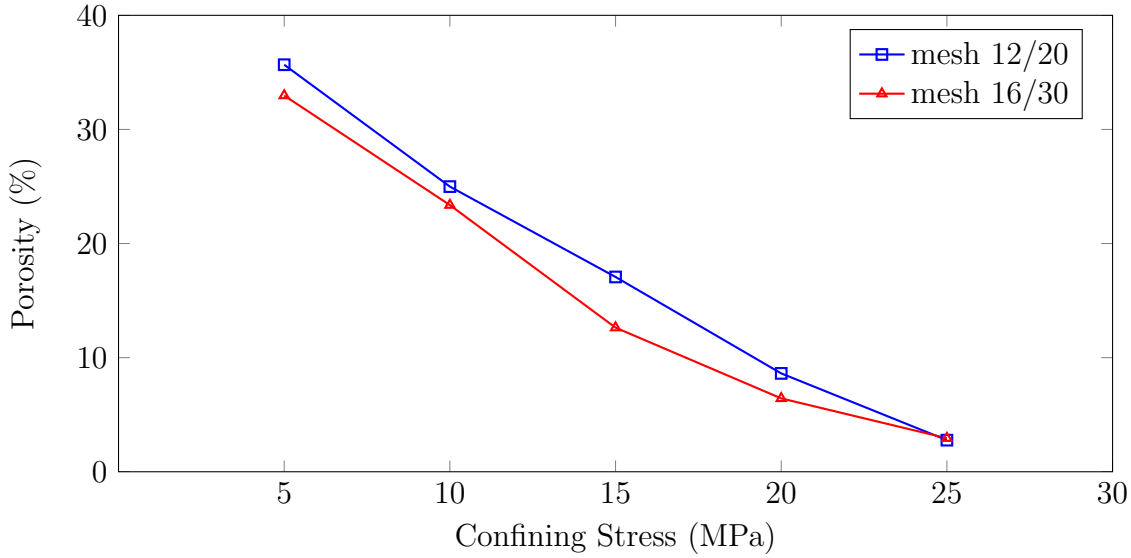

FIGURE 5.3. Porosity versus confining stress for two sample of proppants

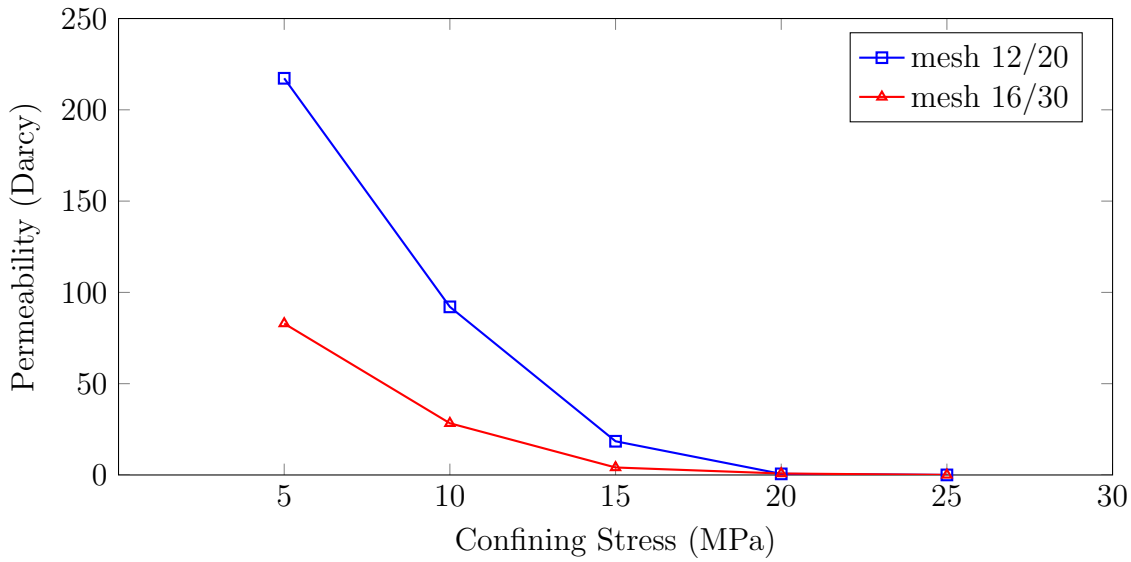

FIGURE 5.4. Permeability versus confining stress for two sample of proppants

fracture width, which means a smaller deformation of the proppants. Fig. 5.6 displays both fracture width values, with the dashed line representing the proppants with higher Young's modulus.

Mesh size 20/40 was included for the following simulations. The porosities and permeabilities, as well as the fracture width obtained are much larger than previous results, subsequently, achieved better fracture conductivity. The manufacturing of

(a)

(b)

FIGURE 5.5. Proppant bed after running the experiment. Soft proppant pack lead to lower rather than higher porosity after running the experiment. High Youngs modulus is critical for proppant functionality.

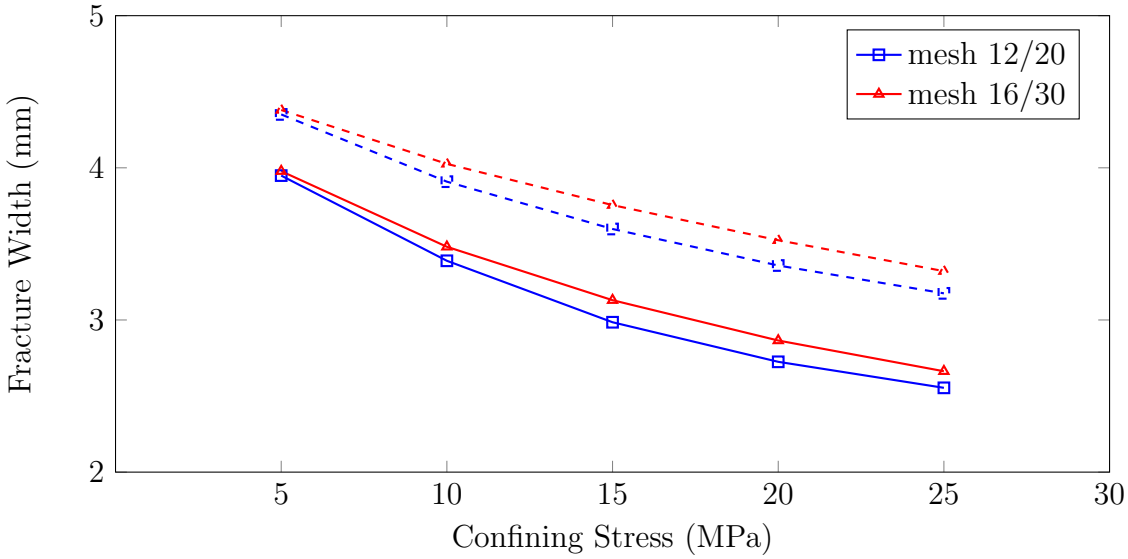

FIGURE 5.6. Comparison between the fracture width for the premilinary sample of proppants and the ones with increased strength

the proppants with various Youngs modulus is currently underway to have effective proppant system for different formation in-situ conditions. The Youngs modulus

is still small if compared to sand, for instance. As a result, permeability values obtained are smaller than regular proppants of the same size.

Proppant size has a significant effect on permeability. For lower values of closure stress, the permeability of the 12/20 proppant is much larger than the other ones. This is the result of larger flow capacity due to the pore sizes. However, this advantage reduces with the increase in closure stress as observed in Fig. 5.8. Coarser proppants have lower strength and can even crush when subjected to higher pressures because of the fewer contact points between them. Other disadvantages include higher settling rate, which means that large proppants will not penetrate in deep fractures, and risk of premature screenout bicause of larger particle size (Economides, 1992). For this reason smaller proppants are more commonly used in the industry.

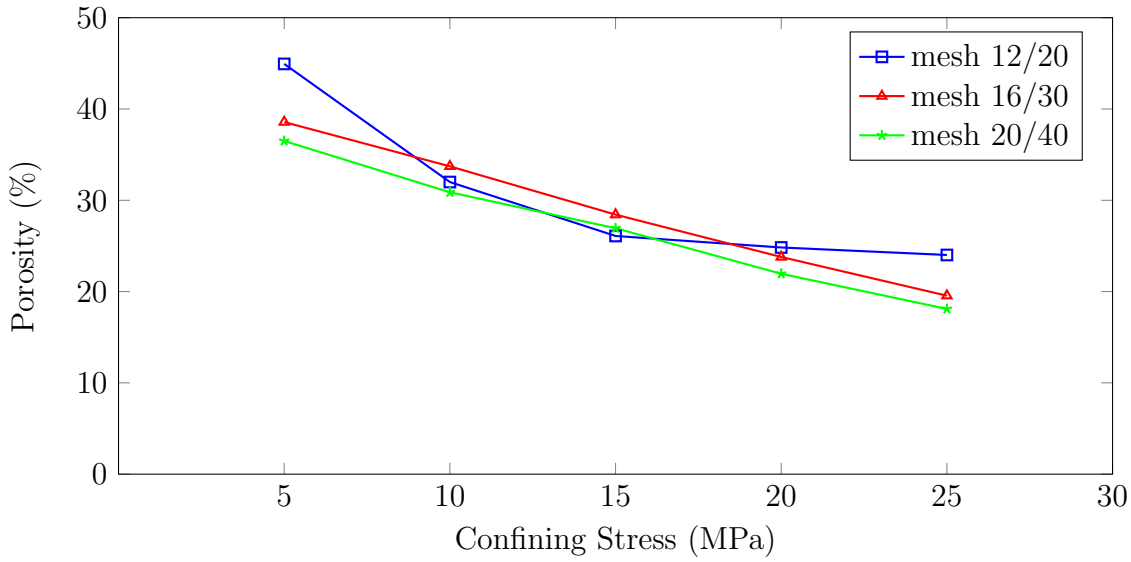

FIGURE 5.7. Porosity versus confining stress for three sample of proppants with increased strength

Te decline of porosity with the increasing confining pressure is almost linear, with exception to the proppants mesh size 12/20. The small sample plus the large

size of the particles may have affected the rearrangement of the pack and do not represent well the proppant bed.

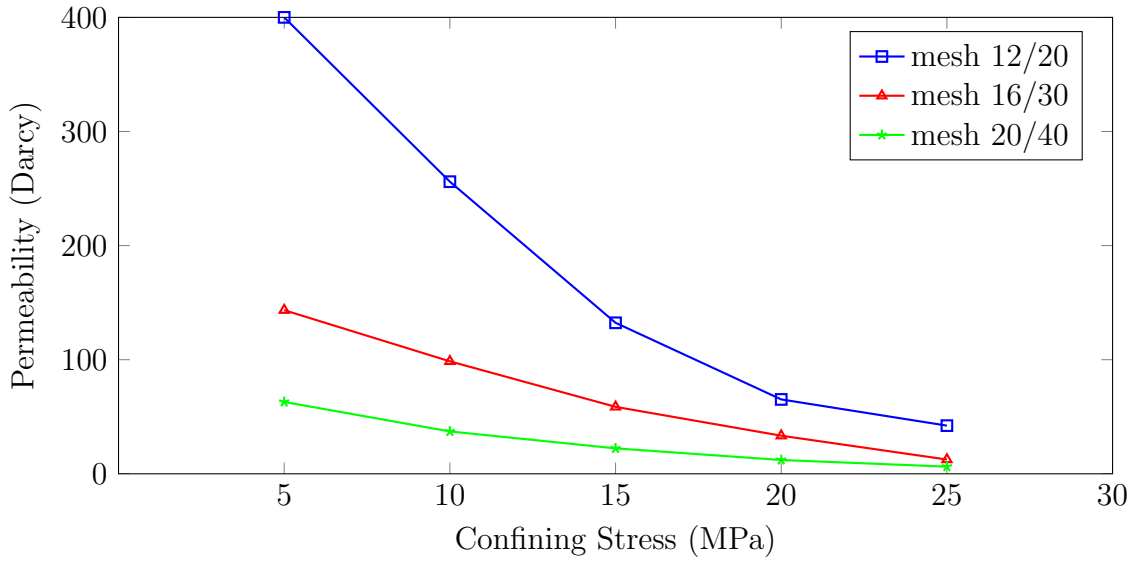

FIGURE 5.8. Permeability versus confining stress for three sample of proppants with increased strength

5.3 Model Verification

A second analysis was performed in order to validate our model. By comparing permeability results with an analytical solution we can measure the accuracy of the model. Carman-Kozeny correlation was chosen for this purpose. The equation is based on power-law, it is widely accepted and is one of the simplest models. It can relate the permeability of the porous medium with porosity. In addition Carman -Kozeny correlation can give reasonable results for very porous, consolidated and anisotropic media (Mauran, Rigaud, and Coudevylle, 2001). There are several modifications of this model for more specific cases, involving different mechanical or geometrical parameters.

$$k = \frac{d^2\phi^3}{72\tau(1-\phi)^2} \tag{5.1}$$

Here, τ is the tortuosity of the porous medium. Tortuosity can be defined as an average elongation of the fluid path. One way to calculate is based on the velocity values (Koponen, Kataja, and Timonen, 1996)

$$\tau = \frac{\langle U_{mag} \rangle}{\langle U_x \rangle} \tag{5.2}$$

where $\langle U_{mag} \rangle$ is the intrinsic velocity over the entire system volume and $\langle U_x \rangle$ is the volumetric average of the velocity component in the flow direction. Fig. 5.9 presents the comparison between the two models, with the dashed line being the analytical result and the continuous line is the numerical value. The tortuosity values obtained were close to one due to the unresolved approach used for the simulations. The fluid path is approximately a straight line.

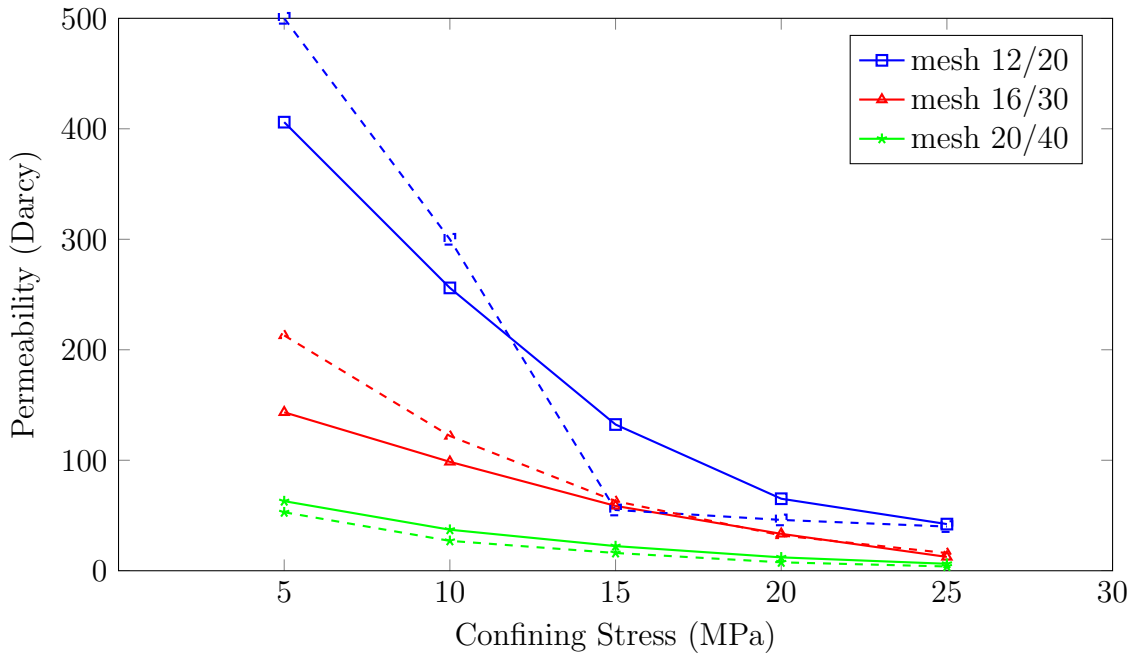

FIGURE 5.9. Comparison between permeability versus confining stress values given by the numerical and analytical models

The results show good agreement between the numerical and the Carman-Kozeny correlation. While for coarser particles the permeability differs, due to

the sudden drop in porosity as explained earlier in this work, for smaller particles the values for the full range of porosities follow the same trend.

5.4 Proppant expansion

After heating the proppants to 90°C we can observe their expansion. The smart proppants are programmed to expand 10% and 20% in size. To capture nonlinear contact between particles and its changes, we need to have a small enough time increments for simulating particles' activation.

5.4.1 Mesh size 12/20

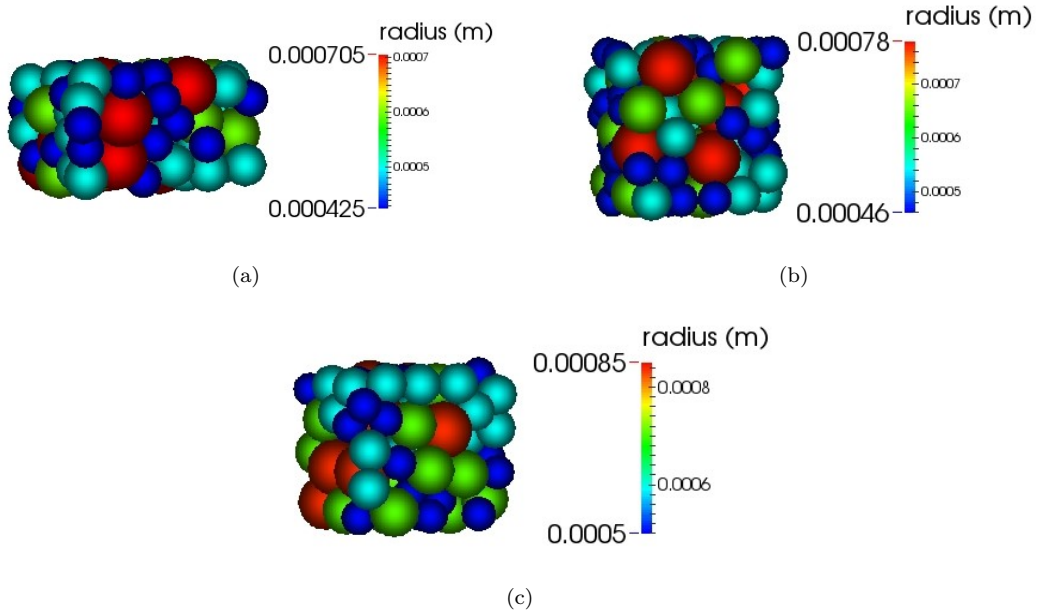

FIGURE 5.10. Example of a 12/20 proppant pack under 20MPa of confining stress a)With no expansion b)Expanding 10% c)Expanding 20%

The expansion of 12/20 mesh size proppants resulted in a large increment in fracture width (Fig. 5.13). The larger increment was at 5MPa, where the width reached 7.78 mm but it did not guaranteed an increase in porosity. For higher confining stresses the porosity is higher for the expanded proppant but there are no big differences between 10 and 20% expansion (Fig 5.11). The permeability of the expanded proppant is also higher in comparison with the not expanded, reaching an incremental of up to 50%.

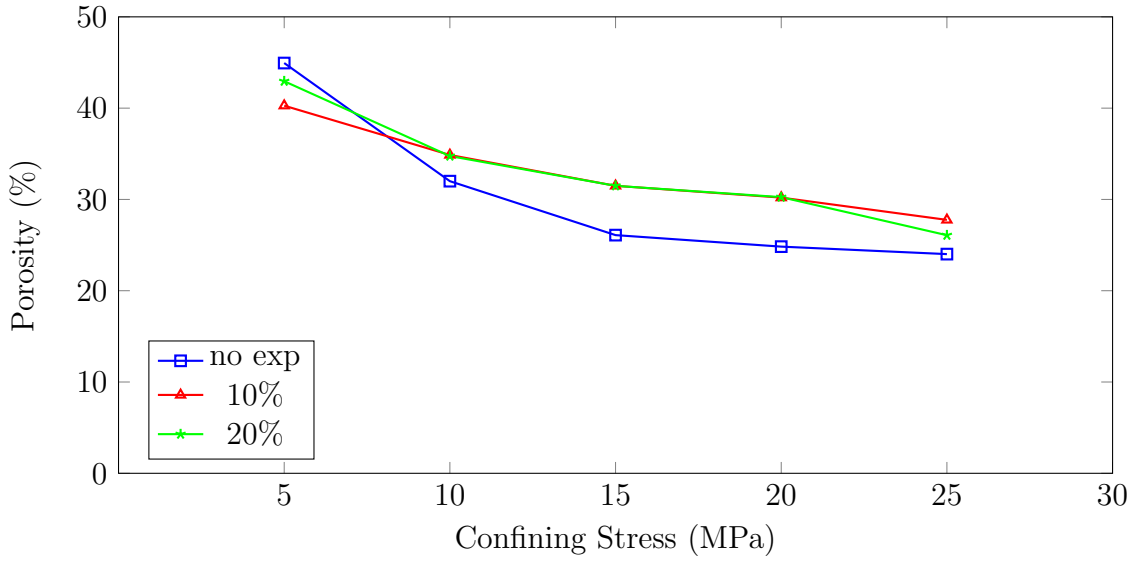

FIGURE 5.11. Porosity of proppants mesh size 12/20 and expanded proppants over a range of confining pressure

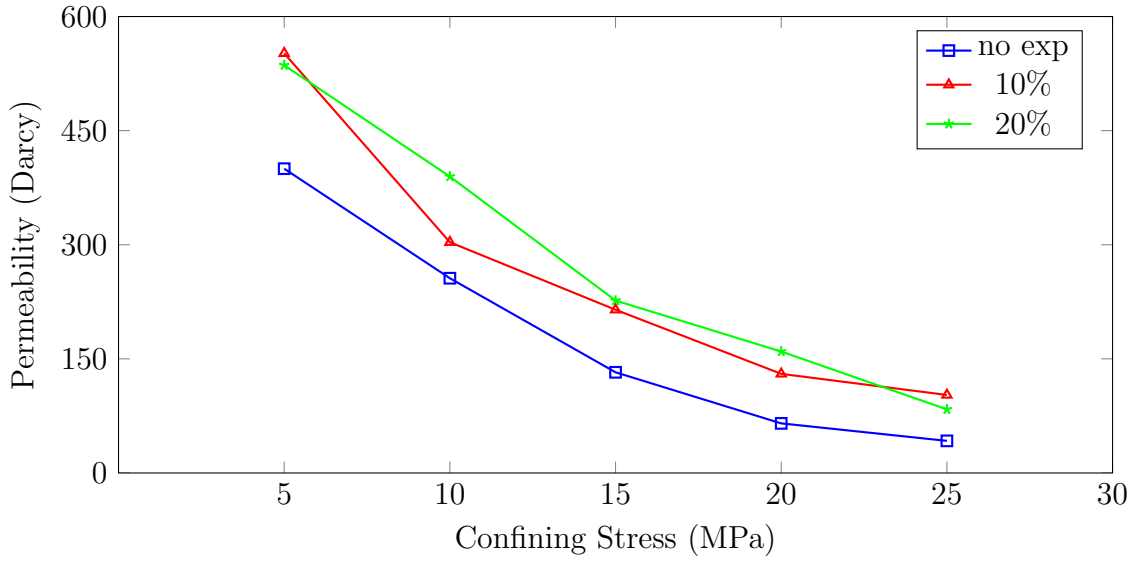

FIGURE 5.12. Permeability of proppants mesh size 12/20 and expanded proppants over a range of confining pressure

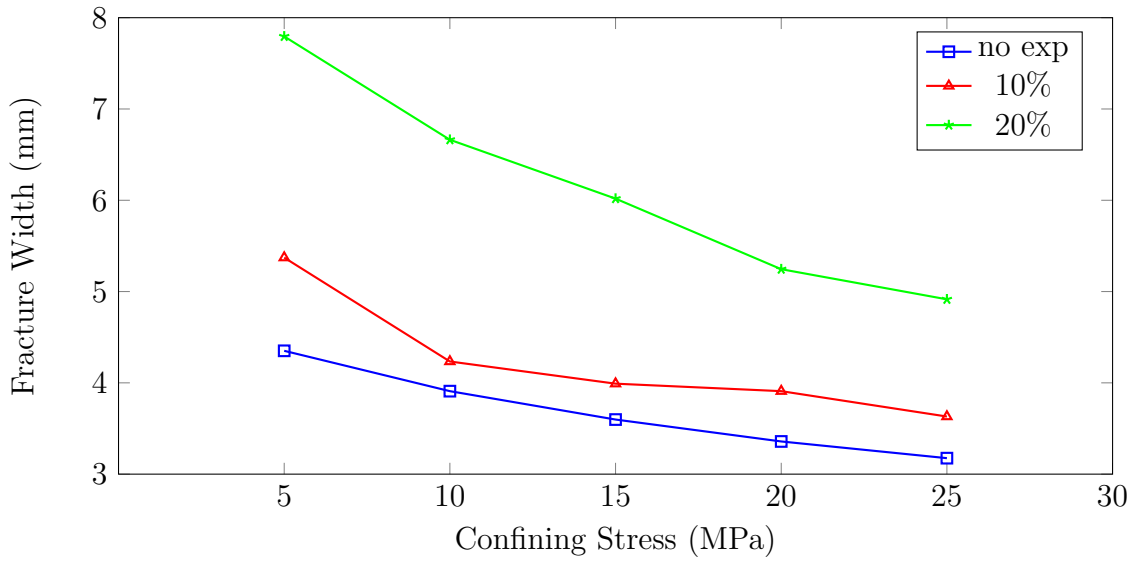

FIGURE 5.13. Fracture width of proppants mesh size 12/20 and expanded proppants over a range of confining pressure

5.4.2 Mesh size 16/30

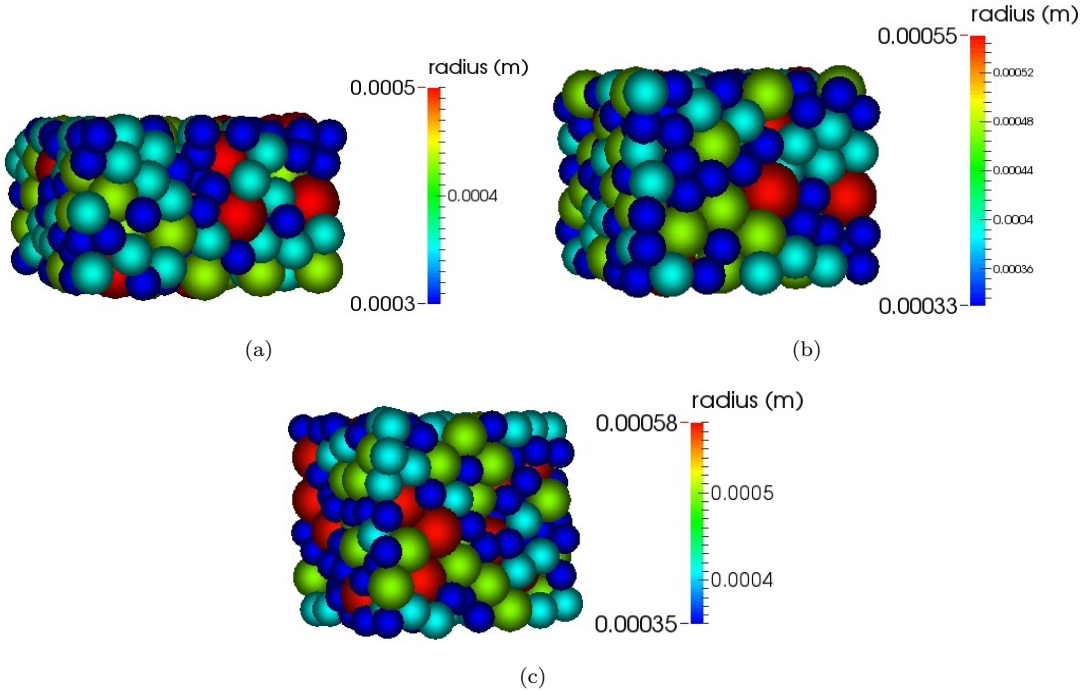

FIGURE 5.14. Example of a 16/30 proppant pack under 20MPa of confining stress a)With no expansion b)Expanding 10% c)Expanding 20%

The results obtained at the 16/30 mesh size simulations follow a better trend. Again, Fig. 5.17 shows that 20% of expansion of the proppant increased the fracture width in 50%, while the 10% expansion only by 10%. Regarding the porosity, the 10% expansion of the proppant resulted in an increase between 2-4% and the 20% leaded to 3-6% increments (Fig. 5.15). Finally, the permeability can increase up to 83% under 5MPa of confining pressure, but as the pressure increase the increment in permeability tend to be around 60% (Fig. 5.16).

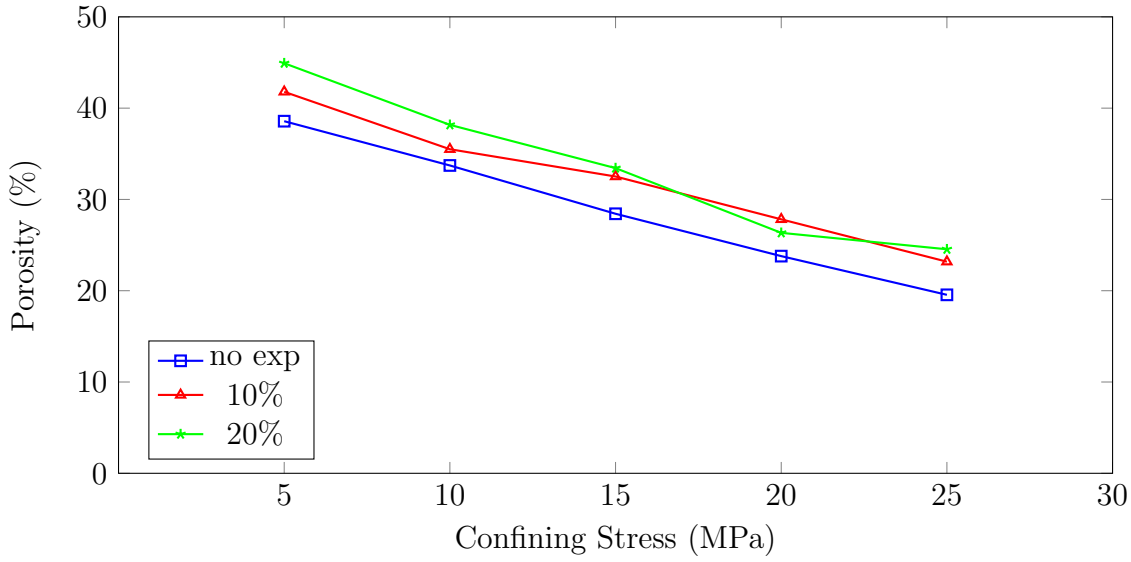

FIGURE 5.15. Porosity of proppants mesh size 16/30 and expanded proppants over a range of confining pressure

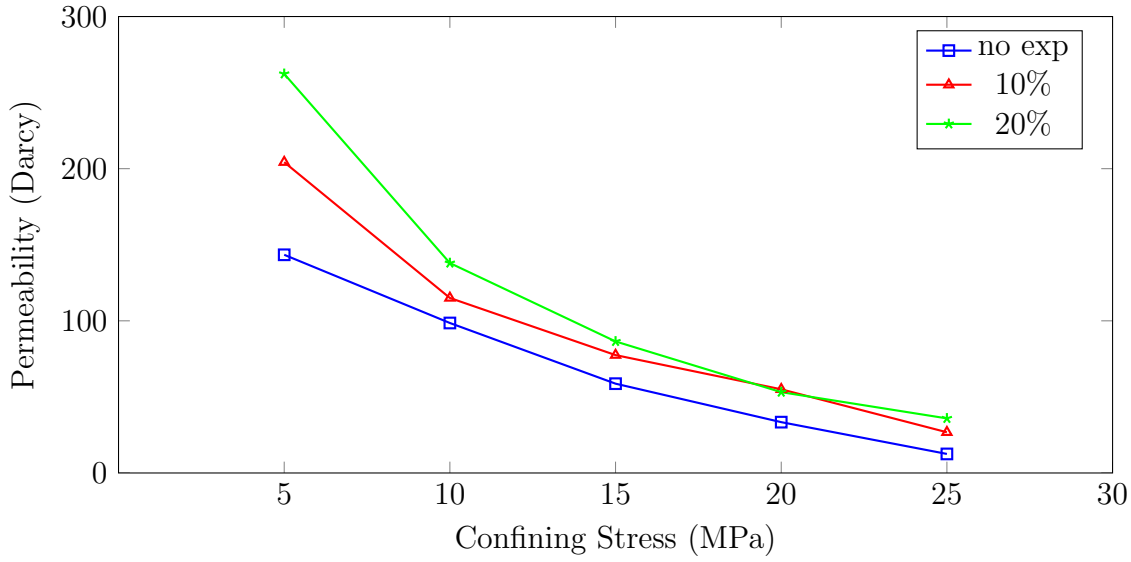

FIGURE 5.16. Permeability of proppants mesh size 16/30 and expanded proppants over a range of confining pressure

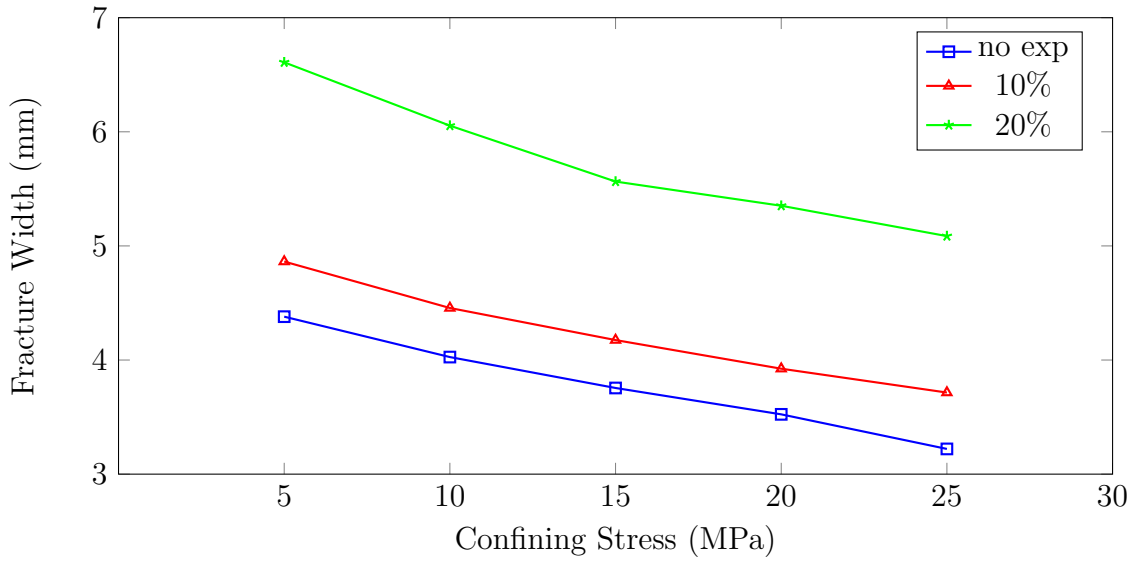

FIGURE 5.17. Fracture width of proppants mesh size 16/30 and expanded proppants over a range of confining pressure

5.4.3 Mesh size 20/40

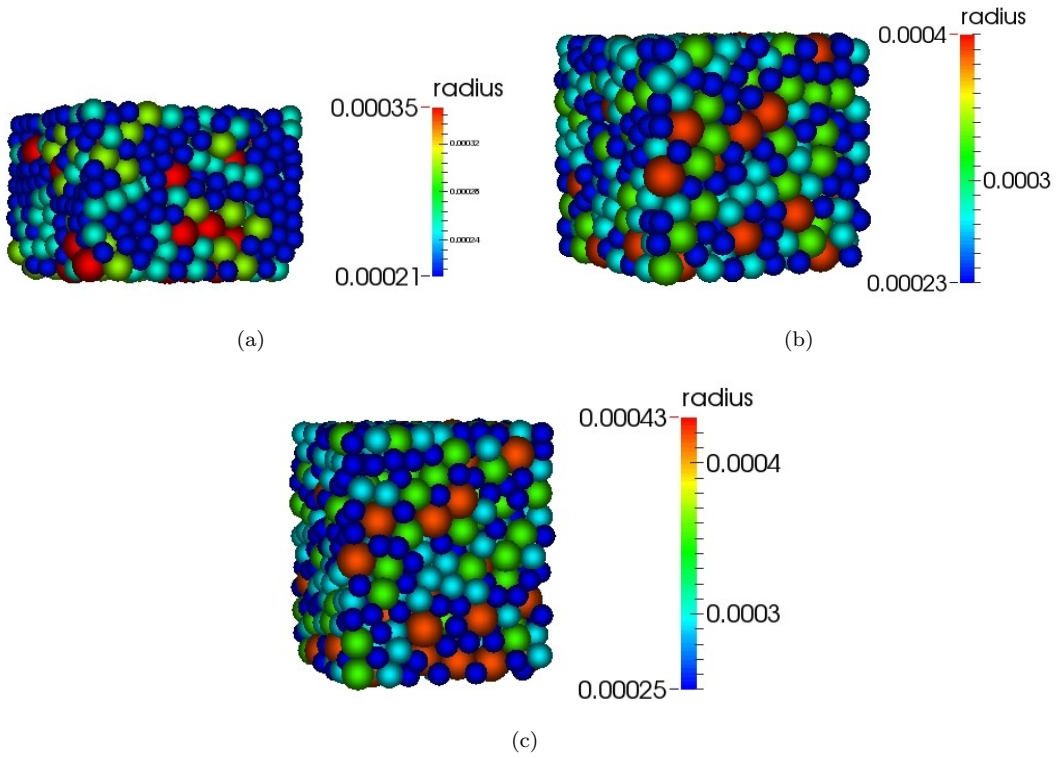

FIGURE 5.18. Example of a 20/40 proppant pack under 20MPa of confining stress a)With no expansion b)Expanding 10% c)Expanding 20%

Porosity plots follow similar trends as the previous ones, with up to 4% increments considering both expansion cases (Fig. 5.19). As presented in Fig. 5.21, the fracture width results show constant increase for the range of confining pressure, with 35% and 65% enlargement for the 10% and 20% expansion, respectively. Lastly, Permeability can increase more than 100% when 25MPa of confining stress is applied, from 6.28 to 14.63 Darcy, for instance. The original permeability was very low, but in general increments are around 30 and 60% for each case.

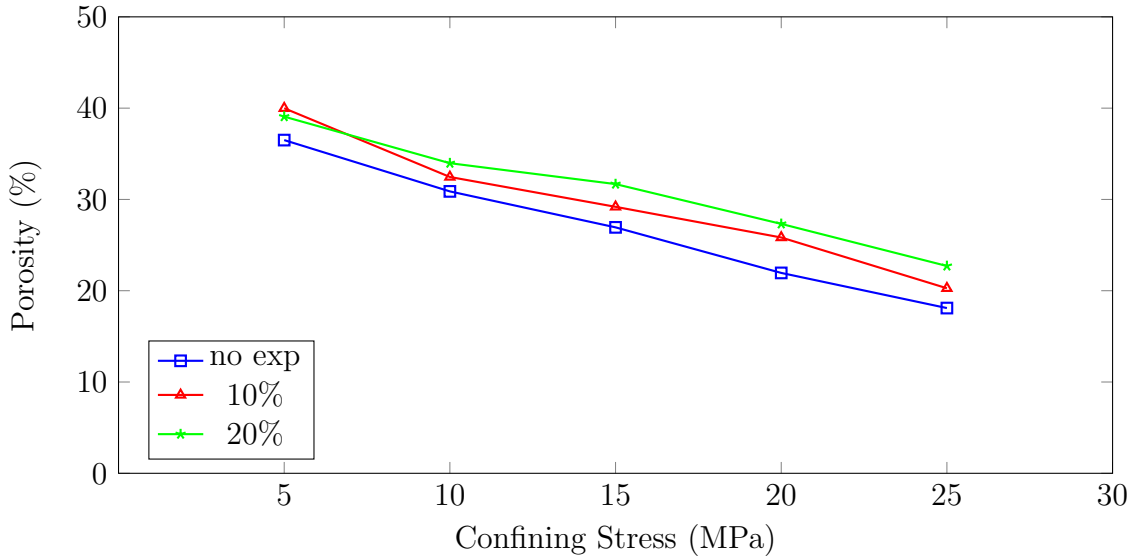

FIGURE 5.19. Porosity of proppants mesh size 20/40 and expanded proppants over a range of confining pressure

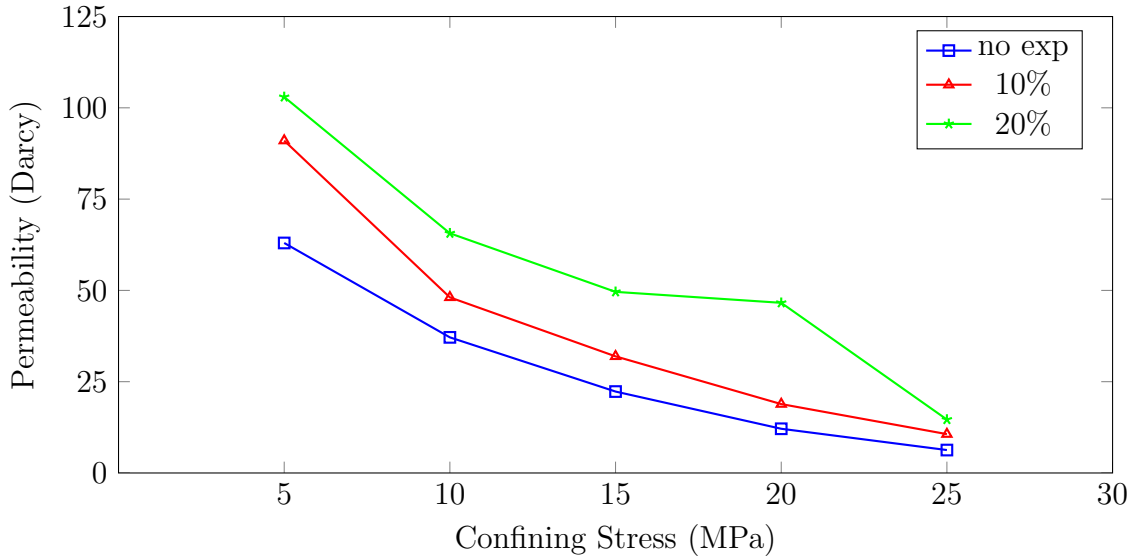

FIGURE 5.20. Permeability of proppants mesh size 20/40 and expanded proppants over a range of confining pressure

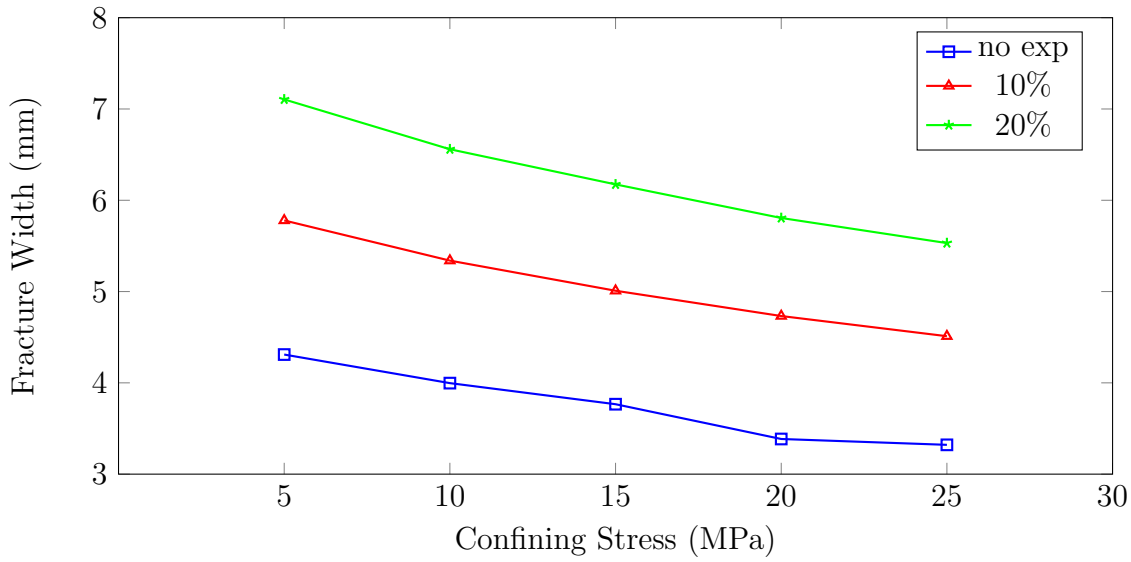

FIGURE 5.21. Fracture width of proppants mesh size 20/40 and expanded proppants over a range of confining pressure

5.5 General Discussion of the Results

The higher stiffness of the material has proved to compensate the large deformations experienced by the original proppant. The shrinkage of the proppant pack volume is reduced, resulting in better fracture conductivity. As expected, porosity and permeability decrease with confining stress.

The results displayed in Figs 5.11, 5.15 and 5.19 show that proppant expansion cause porosity increments of up to 5%, with the 20% expansion increasing slightly more than the 10% expansion. Again, this fact can be caused by the low values of the Youngs modulus, leading to proppant deformations under these high stresses. This suggests that programming the proppant to expand even more will not have strong effects in porous space gains. Although porosity and permeability are distinct physical properties of the solids, they are closely related. Permeability increments were more significant, between 25 to 100%.

While small differences in permeabilities between the cases with 10% and 20% expansion are observed, the fracture width increases considerably, more than 1 mm in all three cases. This implies that the fracture conductivity can be much larger even if there are few gains in permeability. High conductivity fractures not only increases production but also can mitigate sand production, asphaltene deposition, paraffin build up and even reduce scaling tendencies by redistributing the pressure drawdown (Vincent et al., 2002). As anticipated, the stress released during the expansion is enough to cause a small increase in the fracture width, generating bigger pore throats. Wide fractures are less prone to proppant embedment. In addition, proppant size have a big influence in all these properties. Bigger particles leaded to larger values of permeability and porosity but the results were not very consistent, probably due to low number of particles and the rearrangement of the grains. Small size proppants are more commonly used and have the advantage of

penetrating deeper in the fractures, but after the expansion they behave like larger particles.

Permeability values may be underestimated in this study as few cells were used in the CFD simulation. Additionally, the tortuosity is also underestimated and consider almost a straight path for the fluid in the proppant bed. The resolved approach, with particle sizes bigger than the computational grid, could lead to more precise values, however with more computational time.

Chapter 6
Conclusions and Recomendations for Future Work

To prevent reduction in fracture conductivity and enhance production of hydraulically fractured wells, a new type of smart proppant is introduced in this research. A fracture conductivity cell was built to test these proppants and a coupled CFD-DEM model is also presented and verified, to evaluate the proppant pack properties, such as porosity and permeability under uniform confining stress and laminar flow. The main parameters considered for this study were proppant size, stiffness, porosity, permeability, confining pressure and fracture aperture.

Our preliminary laboratory results indicate that the Youngs Modulus and released stress of the SMP have strong influences on the results. Experiments performed in the conductivity cell confirmed preliminary predicts and in good agreement with our numerical model. In order to improve the performance of the proppants, we proposed a range for the value of the Youngs Modulus. Proppant expansion due to temperature can increase permeability up to 100% by only 10% expansion of SMP particles. However little difference was observed between cases with 10% and 20% expansion. The fracture width increased 1 mm in average for all cases, resulting in higher fracture conductivity. Although these values are still smaller than regular proppants, they are a good indication that the smart proppants work and can be improved.

The focus of this work was on testing the viability of the new smart proppant. We verified the porosity and permeability of different sizes of proppant and how much they can increase with expansion. Improvements in either the numerical model and experiments, as well as recommendations for future work include

1. Investigation of proppants with a range of Young's modulus to determine the ideal ones for each formation.

2. Test smaller particles up to mesh 140, providing complete information about the proppant properties.

3. Conduct tests mixing regular proppants (sand) with EP, with different concentrations. This will allow the operation to become more economic viable.

4. Further improvement of the experimental apparatus involve

   (a) Use of fracturing fluid (gel), instead of water, to build a filter-cake and give more realistic results.

   (b) Conduct experiments with shale cores, simulating shale reservoirs and compare with sandstone results

5. Further recommendations of the numerical model shoould include

   (a) Development of the code to model anisotropic expansion of the proppant, which will result in a similar behaviour as the real particles

   (b) Model non-Darcy flow in the fracture. Non-Darcy effects have big impact in the fracture conductivity even in low flow rates.

Bibliography

API RP 61, Recommended Practices for Evaluating Short Term Proppant Pack Conductivity (1989). first edition. Washington, DC: API.

Asala, H.I. et al. (2016). "Why Re-fracturing Works and Under What Conditions". In: *SPE-181516-MS*.

Asgian, M.I., P.a. Cundall, and B.H.G. Brady (1995). "Mechanical Stability of Propped Hydraulic Fractures: A Numerical Study". In: *Journal of Petroleum Technology* 47.3, pp. 203–208. ISSN: 01492136. DOI: 10.2118/28510-PA.

Baghani, M., H. Mohammadi, and R. Naghdabadi (2014). "An analytical solution for shape-memory-polymer EulerBernoulli beams under bending". In: *International Journal of Mechanical Sciences* 84, pp. 84–90. ISSN: 00207403. DOI: 10.1016/j.ijmecsci.2014.04.009. URL: http://linkinghub.elsevier.com/retrieve/pii/S0020740314001325.

Barree, R D et al. (2003). "Realistic Assessment of Proppant Pack Conductivity for Material Selection". In: *Proceedings - SPE Annual Technical Conference and Exhibition*, pp. 2219–2230. DOI: 10.2118/84306-MS. URL: http://www.scopus.com/inward/record.url?eid=2-s2.0-1142301491{\&}partnerID=40{\&}md5=7be9d6d11f11d92fd43ea4e0707160fe.

Blauer, R (1997). "The Detection, Simulation, and Reservoir Performance Impact of Slowly Closing Fractures". In: *Society of Petroleum Engineers*. DOI: http://dx.doi.org/10.2118/37404-MS.

Carrejo, Nick, Mike H Johnson, and D N Horner (2011). "Shape Memory Polymer as a Sand Management Alternative to Gravel Packing". In: *SPE Canadian Unconventional Recources Conference 2011* November.

Chaudhuri, Bodhisattwa, Fernando J. Muzzio, and M. Silvina Tomassone (2006). "Modeling of heat transfer in granular flow in rotating vessels". In: *Chemical Engineering Science* 61.19, pp. 6348–6360. ISSN: 00092509. DOI: 10.1016/j.ces.2006.05.034.

Cole, SW, MW Amundson, and JS Allen (1999). "Remedial proppant consolidation using resin technology". In: pp. 485–490.

Cooke, C E Jr (1973). "Conductivity of Fracture Proppants in Multiple Layers". In: *Journal of Petroleum Technology* 25.9, pp. 1101–1107. ISSN: 01492136. DOI: 10.2118/4117-PA.

– (1975). "Effect of Fracturing Fluids on Fracture Conductivity". In: *Spe*, pp. 1273–1282. ISSN: 01492136. DOI: 10.2118/5114-PA.

Cundall, P.A. and O.D.L. Strack (1979). "A Discrete Numerical Model for Granular Assemblies". In: *Geotechnique* 29.1, pp. 47–65.

Dahi Taleghani, Arash (2010). "Fracture re-initiation as a possible branching mechanism during hydraulic fracturing". In: *44th US Rock Mechanics Symposium and 5th US-Canada Rock Mechanics Symposium*. American Rock Mechanics Association.

Dahi Taleghani, Arash and Jon Olson (2014). "How natural fractures could affect hydraulic-fracture geometry". In: *SPE Journal* 19.01, pp. 161–171.

Deng, Shouchun et al. (2014). "Simulation of shaleproppant interaction in hydraulic fracturing by the discrete element method". In: *International Journal of Rock Mechanics and Mining Sciences* 70, pp. 219 –228. ISSN: 1365-1609. DOI: http://dx.doi.org/10.1016/j.ijrmms.2014.04.011. URL: http://www.sciencedirect.com/science/article/pii/S1365160914001063.

Dewprashad, B T et al. (1999). "Modifying the Proppant Surface To Enhance Fracture Conductivity". In: *Spe Oilfield Chem. Int. Symp. (Houston, 2/16-19/1999) Proc.* 199919, pp. 325–333. DOI: 10.2118/50733-MS. URL: http://search.ebscohost.com/login.aspx?direct=true{\&}db=pta{\&}AN=699248{\&}site=ehost-live.

Di Felice, R. (1994). "The voidage function for fluid-particle interaction systems". In: *International Journal of Multiphase Flow* 20.1, pp. 153–159. ISSN: 03019322. DOI: 10.1016/0301-9322(94)90011-6.

Economides, Michael J (1992). *A practical companion to reservoir stimulation*. Vol. 34. Elsevier.

Fredd, C.N. et al. (2001). "Experimental Study of Fracture Conductivity for Water-Fracturing and Conventional Fracturing Applications". In: *SPE Journal* 6.3, pp. 12–15. ISSN: 1086-055X. DOI: 10.2118/74138-PA.

Kaufman, Phillip B et al. (2007). "SPE 110697 Introducing New API/ISO Procedures for Proppant Testing". In: *Society of Petroleum Engineers*, p. 7. DOI: 10.2118/110697-MS.

Kloss, C. et al. (2012). "Models , algorithms and validation for opensource DEM and CFD-DEM". In: *Pcfd* 12, pp. 140–152. ISSN: 1468-4349. DOI: 10.1504/PCFD.2012.047457.

Koponen, A, M Kataja, and Jv Timonen (1996). "Tortuous flow in porous media". In: *Physical Review E* 54.1, p. 406.

Li, Guoqiang (2014). *Self-Healing Composites: Shape Memory Polymer Based Structures*. Ed. by Inc. John Wiley & Sons, p. 392. ISBN: 1118452445.

Li, J and D J Mason (2000). "A computational investigation of transient heat transfer in pneumatic transport of granular particles.pdf". In: pp. 273–282.

Mader, Detlef (1989). *Hydraulic proppant fracturing and gravel packing*. Vol. 26. 1. Amsterdan, p. 1277. ISBN: 9780444873521. DOI: 10.1016/0920-4105(91)90028-L.

Marpaung, F et al. (2008). "SPE 115653 Measurement of Gel Cleanup in a Propped Fracture W ith Dynamic Fracture Conductivity Experiments". In: 1987, pp. 1–11.

Mattson, E.D. et al. (2014). "Discrete Element Modeling Results of Proppant Rearrangement in the Cooke Conductivity Cell". In: *SPE Hydraulic Fracturing Technology Conference* 61.Cook 1975.

Mauran, S, L Rigaud, and O Coudevylle (2001). "Application of the Carman–Kozeny Correlation to a High-Porosity and Anisotropic Consolidated Medium:

The Compressed Expanded Natural Graphite". In: *Transport in Porous Media* 43.2, pp. 355–376.

McDaniel, B.W. (1986). "Conductivity Testing of Proppants at High Temperature and Stress". In: *SPE California Regional Meeting*. DOI: 10.2118/15067-MS. URL: https://www.onepetro.org/conference-paper/SPE-15067-MS?sort={\&}start=0{\&}q=15067{\&}from{_}year={\&}peer{_}reviewed={\&}published{_}between={\&}fromSearchResults=true{\&}to{_}year={\&}rows=10{\#}.

Milton-tayler, David, Chris Stephenson, and M I Asgian (1992). "Results of a Laboratory Study". In:

Mollanouri Shamsi, MM, Sh Farhadi Nia, K Jessen, et al. (2015). "Conductivity of Proppant-Packs under Variable Stress Conditions: An Integrated 3D Discrete Element and Lattice Boltzman Method Approach". In:

O'Sullivan, Catherine (2011). *Particulate discrete element modelling: a geomechanics perspective*, p. 574. ISBN: 9780415343046.

Penny, G.S (1987). "An Evaluation of the Effects of Environmental Conditions and Fracturing Fluids on the long-term Conductivity of Proppants". In: *Spe exhibition, Dallas*, pp. 229–244.

Shor, Roman J. and Mukul M. Sharma (2014). "Reducing Proppant Flowback From Fractures: Factors Affecting the Maximum Flowback Rate". In: *SPE Hydraulic Fracturing Technology Conference*. DOI: 10.2118/168649-MS. URL: http://www.onepetro.org/doi/10.2118/168649-MS.

Tsuji, Y, T Kawaguchi, and T Tanaka (1993). "Discrete particle simulation of a two-dimensional fluidized bed". In: *Powder Tech.* 77, p. 79.

Versteeg, H and W Malalasekera (2006). *Introduction: Computational Fluid Dynamics Validation for Synthetic Jets*. Vol. 44. 2, pp. 193–193. ISBN: 3175723993. DOI: 10.2514/1.22547. URL: http://www.ncbi.nlm.nih.gov/pubmed/6686412.

Vincent, MC et al. (2002). "Proving It-A Review of 80 Published Field Studies Demonstrating the Importance of Increased Fracture Conductivity". In: *SPE Annual Technical Conference and Exhibition*. Society of Petroleum Engineers.

Xie, Tao (2011). "Recent advances in polymer shape memory". In: *Polymer* 52.22, pp. 4985–5000. ISSN: 00323861. DOI: 10.1016/j.polymer.2011.08.003. URL: http://linkinghub.elsevier.com/retrieve/pii/S0032386111006513.

Yu, a. B. and B. H. Xu (2003). "Particle-scale modelling of gas-solid flow in fluidisation". In: *Journal of Chemical Technology and Biotechnology* 78.2-3, pp. 111–121. ISSN: 02682575. DOI: 10.1002/jctb.788.

Zhang, Jingchen and Jirui Hou (2014). "Theoretical conductivity analysis of surface modification agent treated proppant II Channel fracturing application". In: *Fuel* 165, pp. 28–32. ISSN: 00162361. DOI: 10.1016/j.fuel.2015.10.026. URL: http://linkinghub.elsevier.com/retrieve/pii/S0016236115010261.

Zhou, Z. Y. et al. (2010). "Discrete particle simulation of particlefluid flow: model formulations and their applicability". In: *Journal of Fluid Mechanics* 661, pp. 482–510. ISSN: 0022-1120. DOI: 10.1017/S002211201000306X.

Zhu, H. P. et al. (2007). “Discrete particle simulation of particulate systems: Theoretical developments”. In: *Chemical Engineering Science* 62.13, pp. 3378–3396. ISSN: 00092509. DOI: 10.1016/j.ces.2006.12.089.

Appendix A: Experimental Setup

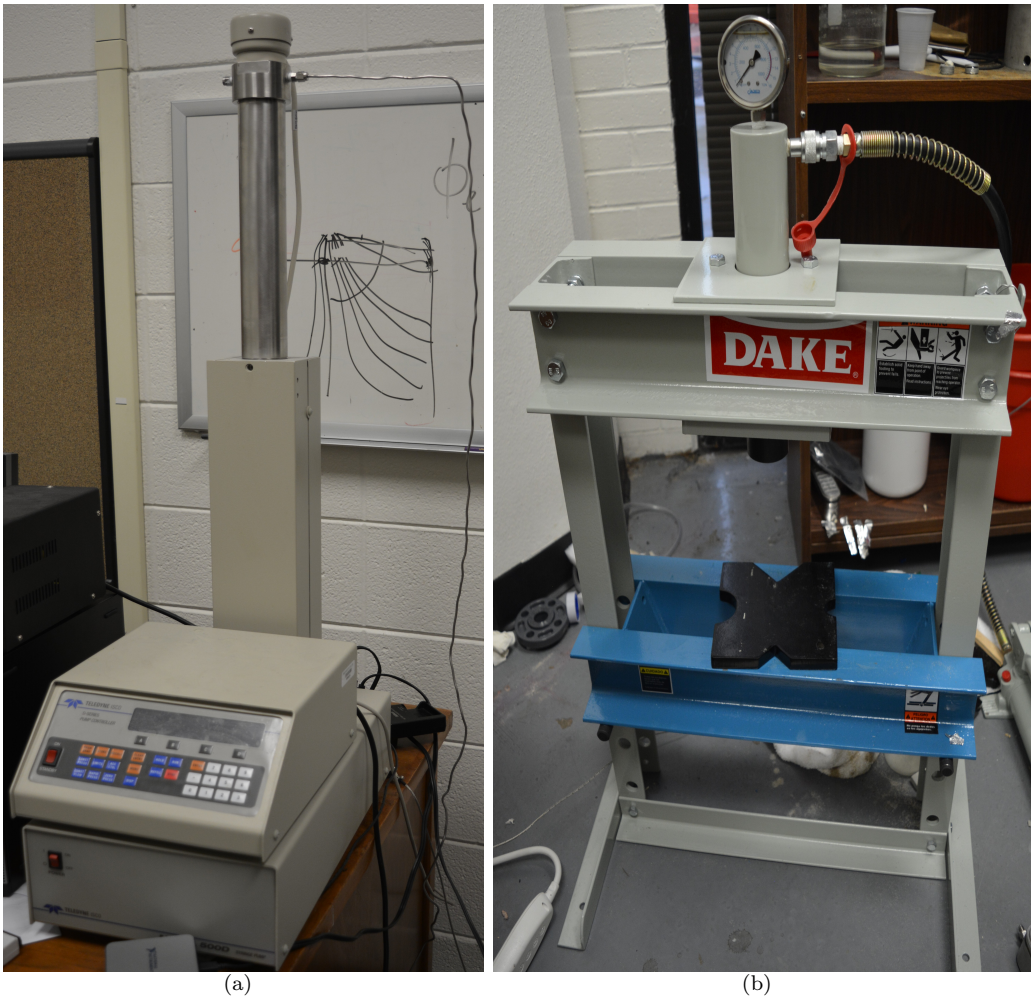

(a) (b)

FIGURE 6.1. Equipments a)Syringe pump to ensure constant flow rate b) Hydraulic press to apply confining pressure

(a)

(b)

FIGURE 6.2. a)Ro-Tap sieve shaker b)Sieves

(a)

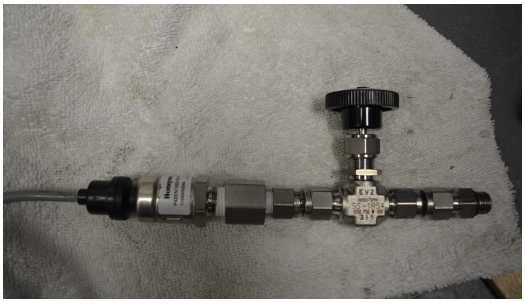

(b)

FIGURE 6.3. a)Deadweight tester used to calibrate the pressure transducers b)Pressure transducer and valve

(a)

(b)

FIGURE 6.4. Data acquisition system a)Pressure; b)Temperature

Vita

Livio Santos was born on October 17, 1987, in Sao Paulo, Brazil. He finished his undergraduate studies in Petroleum Engineering at University of Sao Paulo on December, 2010. From there Livio has been involved in the oil and gas industry, working as drilling engineer and completions engineer for three years. He enrolled for the Master's Program at Louisiana State University in August 2014.